

Generating Global Products of LAI and FPAR From SNPP-VIIRS Data: Theoretical Background and Implementation

Kai Yan¹, Taejin Park², Chi Chen, Baodong Xu, Wanjuan Song, Bin Yang, Yelu Zeng, Zhao Liu, Guangjian Yan³, Yuri Knyazikhin, and Ranga B. Myneni

Abstract—Leaf area index (LAI) and fraction of photosynthetically active radiation (FPAR) absorbed by vegetation have been successfully generated from the Moderate Resolution Imaging Spectroradiometer (MODIS) data since early 2000. As the Visible Infrared Imaging Radiometer Suite (VIIRS) instrument onboard, the Suomi National Polar-orbiting Partnership (SNPP) has inherited the scientific role of MODIS, and the development of a continuous, consistent, and well-characterized VIIRS LAI/FPAR data set is critical to continue the MODIS time series. In this paper, we build the radiative transfer-based VIIRS-specific lookup tables by achieving minimal difference with the MODIS data set and maximal spatial coverage of retrievals from the main algorithm. The theory of spectral invariants provides the configurable physical parameters, i.e., single scattering albedos (SSAs) that are optimized for VIIRS-specific characteristics. The effort finds a set of smaller red-band SSA and larger near-infrared-band SSA for VIIRS compared with the MODIS heritage. The VIIRS LAI/FPAR is evaluated through comparisons with one year of MODIS product in terms of both spatial and temporal patterns. Further validation efforts are still necessary to ensure the product quality. Current results, however, imbue confidence in the VIIRS data set and suggest that the efforts described here meet the goal of achieving the operationally consistent multisensor LAI/FPAR data sets. Moreover, the strategies of parametric adjustment and LAI/FPAR evaluation applied to SNPP-VIIRS can also be employed to the subsequent Joint Polar Satellite System VIIRS or other instruments.

Index Terms—Earth System Data Record (ESDR), fraction of photosynthetically active radiation (FPAR), leaf area index (LAI), Moderate Resolution Imaging Spectroradiometer (MODIS), spectral invariants, Visible Infrared Imaging Radiometer Suite (VIIRS).

Manuscript received August 30, 2017; revised October 20, 2017; accepted November 15, 2017. This work was supported in part by the National Natural Science Foundation of China through the Chinese Key Program under Grant 41331171 and in part by the National Aeronautics and Space Administration Earth Science Division under Grant NNX14AP80A, Grant NNX14A171G, and Grant NNX16AO34H. (Corresponding authors: Taejin Park; Guangjian Yan.)

K. Yan, W. Song, Z. Liu, and G. Yan are with the State Key Laboratory of Remote Sensing Science, Faculty of Geographical Science, Beijing Normal University, Beijing 100875, China (e-mail: kaiyan.earthscience@gmail.com).

T. Park, C. Chen, B. Xu, Y. Knyazikhin, and R. B. Myneni are with the Department of Earth and Environment, Boston University, Boston, MA 02215 USA (e-mail: parktj@bu.edu).

B. Yang is with the College of Electrical and Information Engineering, Hunan University, Changsha 410082, China (e-mail: binyang@hnu.edu.cn).

Y. Zeng is with the Department of Global Ecology, Carnegie Institution for Science, Stanford, CA 94305 USA (e-mail: zengyelu@163.com).

Color versions of one or more of the figures in this paper are available online at <http://ieeexplore.ieee.org>.

Digital Object Identifier 10.1109/TGRS.2017.2775247

I. INTRODUCTION

THE launch of the Moderate Resolution Imaging Spectroradiometer (MODIS) instruments onboard Terra and Aqua satellites opened a new era in remote sensing of the earth system by allowing for rich spectral and angular sampling of the reflected and emitted radiation field [1], [2]. Supported by sound cooperation mechanisms, MODIS science teams have been routinely producing, validating, evaluating, and distributing more than 40 high-quality science products of earth system parameters since 2000. During the past 17 years, the series of MODIS products has unprecedentedly supported a broad range of studies of the earth environment and climate changes [3]–[5], and the quality of these products has been evaluated by both direct validation with ground measurements and intercomparison with other data sets [6], [7].

Given the fact that the MODIS instruments have operated significantly beyond their design lifetime of six years, the calibration team has observed obvious degradations [8]. It is important to realize that the MODIS instruments will be retired in the upcoming several years although constant and dedicated efforts have been made to maintain the product quality [9]. In this context, the Visible Infrared Imaging Radiometer Suite (VIIRS) instrument was designed with a strong MODIS heritage and has the goal of ensuring long-term continuity of the valuable Earth System Data Records (ESDRs) [10]–[12]. The VIIRS was planned to be one of the payloads of the Suomi National Polar-orbiting Partnership (SNPP) and Joint Polar Satellite System (JPSS) satellites. The on-orbit SNPP-VIIRS provides a critical bridge between the observations from the Earth Observing System (EOS) and the JPSS [13].

Leaf area index (LAI) [14] and the fraction of photosynthetically active radiation (FPAR) (0.4–0.7 μm) absorbed by vegetation [15] are two key biophysical variables that play important roles in most models of climate, hydrology, biogeochemistry, and ecosystem productivity by characterizing vegetation canopy structure and energy absorption capacity [16]–[18]. Over the last decades, a number of global LAI/FPAR products with varying temporal–spatial resolutions have been retrieved from satellite observations [19]–[24]. Table I lists the characteristics of five well-known products and the upcoming VIIRS product. Among them, the MODIS product is noteworthy, because its radiative transfer (RT)-based algorithm, unlike other algorithms such as GLASS and

TABLE I
LONG-TERM GLOBAL LAI/FPAR PRODUCTS FROM REMOTE SENSING DATA

Products	Sensor	Time Period					Temporal Frequency	Spatial Resolution	Algorithm	
		1980	1990	2000	2010	2020				
MODIS-LAI/FPAR	Terra-MODIS			2000		Now	8-day & 4-day	500m & 1km	LUT based on 3D RT	
	Aqua-MODIS			2002		Now				
LAI/FPAR 3g	AVHRR	1981			2011		15-day	1/12°	ANN trained with MODIS LAI/FPAR	
GLASS LAI	AVHRR	1982			2001		8-day	0.05°	GRNN trained with CYCLOPES and MODIS LAI	
	Terra-MODIS			2001		Now	8-day	0.05° & 1km		
CYCLOPES-LAI/FPAR	SPOT-VGT			1999		2007	10-day	1/112°	ANN trained with 1D RT	
GEO-LAI/FPAR	SPOT-VGT			1999		2014	10-day	1km	ANN trained with CYCLOPES and MODIS LAI/FPAR	
	PROBA-V					2014		10-day		1km & 1/3km
VIIRS LAI/FPAR	SNPP-VIIRS					2012		8-day	500m	LUT based on 3D RT
	JPSS-VIIRS					2017		8-day	500m	

LUT, RT, GRNN and ANN stand for “Look-Up-Table”, “Radiative Transfer”, “General Regression Neural Network” and “Artificial Neural Network”, respectively.

GEOV1 that are based on artificial neural networks, does not require benchmark LAI/FPAR products. The latest version (Collection 6, C6) of MODIS LAI/FPAR has been well tested and is freely available [25], [26]. With the end of MODIS in sight, there is now an urgent need to continue the LAI/FPAR data series from other satellite observations.

Although the VIIRS was designed to be considerably similar to MODIS, previous studies have shown that the discrepancies between the two sensors cannot be ignored [27]–[29]. This makes it impossible to apply MODIS algorithms to VIIRS data. The MODIS LAI/FPAR algorithm requires the selection of sensor-specific values of configurable parameters [30]. Previous efforts of implementing this algorithm to Advanced Very High Resolution Radiometer and Landsat data indicate that the discrepancies (e.g., spectral response, spatial resolution) between sensors will result in inconsistent LAI/FPAR products if the parameters are not adjusted specifically [31]–[33]. Therefore, the primary objective of this paper is to adjust the lookup tables (LUTs) of this algorithm to address the differences between the MODIS and VIIRS sensors. Our secondary objective is to evaluate the generated VIIRS LAI/FPAR test products through comparisons with the MODIS C6 data set.

This paper is organized as follows. The theoretical background is introduced in Section II and Appendix A. Section III and Appendix B detail the methodologies for adjusting the parameters and evaluating the generated VIIRS LAI/FPAR. The results, including the comparability of MODIS and VIIRS surface reflectance (SR) data sets and the parameterization specified for VIIRS, are detailed in Section IV. Finally, Section V describes the characteristics of the global

VIIRS LAI/FPAR data set and shows the results of a preliminary evaluation on it. Conclusions are presented in Section VI.

II. THEORETICAL BACKGROUND

The proposed VIIRS LAI/FPAR algorithm is based on the heritages of the long-term operational practice and theoretical studies. The two key heritages are: 1) a mature 17-year-long MODIS LAI/FPAR operational algorithm which is based on the 3-D RT model and LUT-based inversion strategy and 2) a physically and practically proven procedure for achieving intersensor consistency.

A. MODIS LAI/FPAR Algorithm

The MODIS LAI/FPAR algorithm ingests bidirectional reflectance factors (BRFs) at the red and near-infrared (NIR) bands, their uncertainties, sun-sensor geometry, and a biome classification map [30]. It consists of a main algorithm that is based on the 3-D RT equation and a backup algorithm that uses empirical relationships between normalized difference vegetation index (NDVI) and LAI/FPAR fields. The algorithm finds the candidates of LAI/FPAR by comparing observed BRFs with those evaluated from model-based entries stored in the LUT. All canopy/soil patterns for which modeled and observed BRFs differ within a specified level of uncertainty are considered as acceptable solutions. The mean value and the dispersion of these solutions are reported as retrieval and its uncertainty, respectively. A biome map is another important input, in which global vegetation is classified into eight biomes (B1: grasses and cereal crops; B2: shrubs; B3: broadleaf crops;

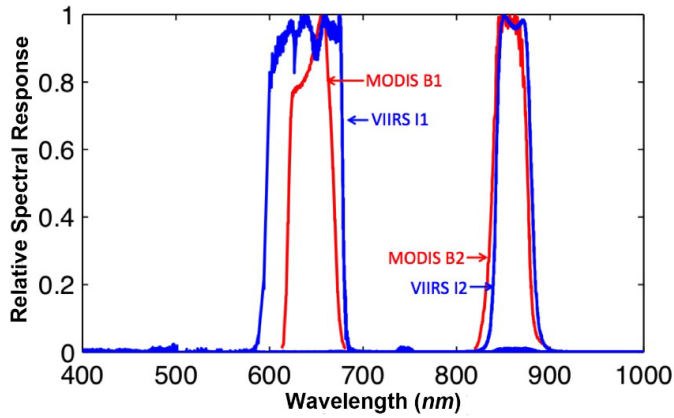


Fig. 1. RSR curves of VIIRS and MODIS red (VIIRS-I1 and MODIS-B1) and NIR (VIIRS-I2 and MODIS-B2) bands. The data for MODIS and VIIRS are available at <http://mst.gsfc.nasa.gov/calibration/parameters> and <http://www.star.nesdis.noaa.gov/jpss/VIIRS.php>, respectively.

B4: savannas; B5: evergreen broadleaf forests; B6: deciduous broadleaf forests; B7: evergreen needleleaf forests; and B8: deciduous needleleaf forests). With simplifying assumptions and standard constants that are assumed to vary only with biome, the biome map, as prior knowledge, can reduce the number of unknowns in the “ill-posed” inverse problem [34]. To reduce the impact of day-to-day artificial variations in SRs that are due to cloud and residual atmospheric effects, the daily retrievals are composited over four-day or eight-day period by selecting the LAI/FPAR corresponding to the maximum FPAR value.

The algorithm path is the key quality assessment (QA) flag that provides information about the overall quality of the retrievals. It includes four types of algorithm paths: the main algorithm without saturation (Main), the main algorithm with saturation (Main-S), the backup algorithm due to bad sun-sensor geometry (BackUp-G), and the backup algorithm due to other reasons (e.g., large uncertainties in reflectance) (BackUp-O). The Main algorithm outputs retrievals with high precision when LAI is low. The Main-S outputs retrievals with moderate precision when LAI is high, and thus, the reflectance has low sensitivity to LAI. In the case of main algorithm failure, low-precision retrievals are obtained from the empirical backup algorithm [35], [36]. Therefore, the retrieval rate of the main algorithm [retrieval index (RI)] is the main quality indicator of MODIS LAI/FPAR products.

B. Characteristics of the VIIRS Instrument

The same as Aqua, the SNPP is an afternoon sun-synchronous satellite with an altitude of approximately 824 km and a 16-day repeat cycle of data collection. Both MODIS and VIIRS are cross-track scanning radiometers (whiskbroom) that measure the globe in multispectral bands [37]. MODIS has 36 bands and VIIRS has 22 bands. Fig. 1 compares the relative spectral responses (RSRs) of the red and NIR bands between the two sensors. It is apparent that VIIRS has an NIR-band RSR that is similar to that of MODIS, with almost the same bandwidth (0.039 versus 0.036 μm) and a

slightly right-shifted center band (0.865 versus 0.859 μm). However, the RSRs of the MODIS and VIIRS red bands show an obvious difference. At this band, VIIRS has a broader bandwidth, with the full-width at half-maximum (FWHM) ranging from 0.60 to 0.68 μm , compared with MODIS’s FWHM (0.62–0.67 μm). The centers of red band for VIIRS and MODIS are 0.639 and 0.645 μm , respectively. Differences in sensor spectral bands result in a differential sensitivity of the sensor’s spectral response functions to the impacts of atmospheric conditions and reflection from the ground [32]. Thus, the BRF data sets from MODIS and VIIRS have discrepancies in both BRF precision and magnitude, which makes it difficult to directly apply MODIS’s LUTs for VIIRS LAI/FPAR retrieval.

VIIRS scans the earth at a view angle ranging between $\pm 56.28^\circ$ for a wider swath of 3000 km than the MODIS’s swath of 2330 km [38]. Therefore, VIIRS has the ability to cover the globe daily with no gap between orbits, which cannot be achieved by MODIS. The larger swath coverage results in more daily observations of VIIRS, which provides the benefits for LAI/FPAR retrieval. Because of the earth curvature and the whiskbroom mechanism, MODIS pixels grow by a factor of six from nadir to edge of scan, whereas VIIRS restricts the pixel to about twofold growth using an onboard aggregation scheme. Many applications have been reported to benefit from VIIRS’s near-constant resolution [39]. The geometric instantaneous fields of views (GIFOVs) of VIIRS and MODIS red and NIR bands are 375 and 250 m, respectively, and are gridded at 500 m as the input of LAI/FPAR retrieval. Note that the measured BRF at pixel scale also depends on the spatial resolution [32]. Therefore, the GIFOV difference is another potential reason for the discrepancies between MODIS and VIIRS BRFs. The nonlinear effects in the LAI-BRFs relationship should be addressed in the VIIRS LAI/FPAR algorithm development.

C. Theory of Spectral Invariants

RT in vegetation canopies can be seen as a stochastic process, i.e., interacting photons can either be scattered or absorbed by a phytoelement [40]. The probability of a scattering event, or single scattering albedo (ω_λ), depends on the wavelength and is a function of the leaf biochemical constitution. However, the probability that a photon will collide with elements again is determined by the structure of the canopy rather than the photon frequency or the optics of the canopy [41]. Reference [42] proposed the “p-theory,” or “spectral invariants theory,” that describes the unique positive eigenvalue of the RT equation as the product of the leaf albedo and a wavelength-independent parameter (p). This theory laid the foundation for the synergistic LUT-based LAI/FPAR algorithm, which has been successfully implemented in the MODIS operational algorithm. To provide a clear interpretation of how p is related to canopy structure, [43] defined p as the recollision probability, the conditional probability that a photon scattered by a phytoelement will interact again within the canopy. Furthermore, [44] proposed the concept of the directional area scattering function (DASF) that is

defined as the BRF of a canopy with nonabsorbing leaves ($\omega_\lambda = 1$) that is bounded underneath by a nonreflecting surface. Note that, the DASF is also determined only by the canopy structure, rather than the wavelength. By introducing the average recollision probability p_A [40], [45], the BRF of vegetation canopies bounded at the bottom by black soil can be expressed as

$$\text{BRF}_\lambda(\Omega_O, \Omega) = \text{DASF}(\Omega_o, \Omega) \cdot \frac{\omega_\lambda \cdot (1 - p_A)}{1 - \omega_\lambda \cdot p_A}. \quad (1)$$

The spectral invariant principle is an important concept, because knowing the invariants of the canopy and the SSA of an average phytoelement at any wavelength makes it possible to reconstruct the radiation field of the canopy at any wavelength [46], [47]. Note that for vegetation canopies with a dark background or for sufficiently dense vegetation where the impact of the canopy background is negligible, the DASF can be directly retrieved from spectral BRF without the use of canopy reflectance models, prior knowledge, or ancillary information regarding the leaf optical properties [44].

The formulation of (1) permits decoupling of the structural and radiometric components of any optical sensor signal, which is the theoretical foundation of optimizing configurable parameters to achieve intersensor consistency in multisensor LAI/FPAR retrievals. Thus, the MODIS LAI/FPAR algorithm is applicable to any optical sensor by selecting the proper sensor-specific values of SSA. The SSA is also a function of the spatial scale, and therefore, it accounts for the variation in BRFs not only with sensor spectral characteristics but also with sensor spatial resolution [32]. Equation (1) shows the nonlinear relationship between BRF and SSA if the canopy structure parameters (e.g., LAI) are constant. However, it is apparent that the BRF_λ is an explicit function of SSA and, if canopy structure parameters and background reflectance are constant, is strictly monotonically increasing. With this relationship, we expect that the direction of SSA changes should agree with that of BRF changes to obtain a consistent LAI/FPAR retrieval. This theoretical prediction can be used to inspect the results of parametrical adjustment.

D. Inverse Problem and Stabilized Precision

Error-free measurements delivering sufficient information content are generally not available in practice. Thus, the retrieval of LAI/FPAR from satellite data cannot be achieved through a one-to-one relationship but should be treated as an “ill-posed” problem [32]. Both the wavelength-dependent observation and model precisions $\sigma_{M,\lambda}$ and σ_λ (Appendix A) must be taken into account when comparing measured and modeled BRFs. Ignoring the model precision in the retrieval algorithm can cause a destabilization of the retrieval process. Reference [48] introduced a stabilized precision δ_λ , which prevents the destabilization and minimizes the impact of model and observation precisions on LAI/FPAR retrievals. The stabilized precision is a function of $\sigma_{M,\lambda}$ and σ_λ . The LAI/FPAR algorithm uses this stabilized precision to select acceptable solutions, i.e., all canopy/soil parameters for which modeled and measured BRFs agree

within the stabilized precisions. A detailed mathematical justification of this procedure is presented in [48] and [49].

In the MODIS/VIIRS retrieval approach, the atmospherically corrected spectral surface BRFs are treated as independent random variables with finite variances (precisions) σ_λ . The deviations, $\varepsilon_\lambda = (r_\lambda - m_\lambda)/\delta_\lambda$, $\lambda = \text{band } 1, \text{band } 2, \dots, \text{band } n$, between measured r_λ and simulated m_λ spectral BRFs are assumed to follow the Gaussian distribution. The random variable $\chi_\delta^2[r-m] = \sum_1^n \varepsilon_k^2$ has a chi-square distribution. The inequality $\chi_\delta^2 \leq n$ indicates good precision.

The operational MODIS/VIIRS algorithm uses BRFs at two spectral bands. It selects all canopy/soil parameters for which modeled $r_{M,\lambda}$ and measured r_λ spectral BRFs agree within the stabilized precisions, i.e., satisfy the inequality $\chi_\delta[r-r_M] \leq 2$. Let $m_M = (m_{M,1}, m_{M,2})$ represent model predicted BRFs. $\chi_\delta^2[r-r_M]$ follows the Minkowski inequality [50], which shows that χ_δ depends on how the modeled BRFs differ from both the true BRFs and the observed BRFs, that is

$$\chi_\delta[r-r_M] \leq \chi_\delta[r-m] + \chi_\delta[r_M-m_M] + \chi_\delta[m-m_M]. \quad (2)$$

Indeed, the use of very accurate model, i.e., $m_{M,\lambda} = m_{\text{true},\lambda}$, maximizes the term $\chi_\delta[m-m_M]$. This may cause a “true” LAI does not pass the comparison test $\chi_\delta[r-r_M] \leq 2$. This term vanishes if one uses a model that tends to simulate the measurements, i.e., $m_{M,\lambda} = m_\lambda$. This, however, increases the contribution of the term $\chi_\delta[r_M-m_M]$. The calibration, therefore, is reduced to finding an SR model that optimally approximates the observed and true spectral BRFs [51]. It is apparent that the solution of this problem depends on model and observation uncertainties. Input data and their uncertainties are, “in general, the minimal information necessary to construct approximate solution for ill-posed problems” [52]. Therefore, our second adjustable parameter is the stabilized precision, which actually accounts for the varying information content of the remote sensing observations and the model uncertainty [32], [33].

III. METHODOLOGY

A. Investigation of the Surface Reflectance

We first investigated the VIIRS SR: 1) to assure comparability of VIIRS BRF precision with MODIS and 2) to quantify BRF differences between MODIS and VIIRS SR data sets. The daily SR data for SNPP-VIIRS (VNP09GA V1) [53] and Aqua-MODIS (MYD09GA C6) [54] during the period July 4–11, 2015 were employed in this analysis. Selected tiles, dominant of the eight biome types, were used for precision examination, and global data sets were used for BRF difference quantification. To achieve a good measure of BRF precisions and their differences, only best quality observations were used, i.e., cloud/adjacent–cloud free, snow free, aerosol not high, and cirrus free. Discrepancy in sun-sensor geometry between MODIS and VIIRS was minimized by only including minimally different observations (a solar zenith angle (SZA) difference of $<2.5^\circ$, a solar azimuth angle difference of $<5^\circ$,

a sensor zenith angle difference of $<5^\circ$, and a sensor azimuth angle difference of $<5^\circ$.

The relative stabilized precisions (RSPs) of input BRFs are practically unmeasurable. Based on previous works [48], [55], [56], we characterized the precision of BRFs by the coefficient of variation (CV) of the strictly quality controlled daily BRFs over these pixels who have almost constant LAI values as

$$CV = S/\mu \quad (3)$$

where S is the standard deviation and μ is the mean value during eight-day period. Thus, the precision comparability was examined by comparing the CVs of BRFs rather than estimating the RSPs. The VIIRS/MODIS observations, if there were at least four daily SRs with best quality during the eight-day period, were used in the precision comparison. Uncertainties in BRFs of these pixels with best quality were, therefore, due to incomplete atmospheric correction and not due to improper cloud screening or instrumental anomalies. For the time being, it was assumed that the surface was unchanged over the measurement period of eight days and that the sun-sensor geometry impact was minimal.

B. Solving the Optimization Problem

The theory of spectral invariants allows the possibility of transplanting the MODIS LAI/FPAR algorithm to VIIRS by selecting the proper values of SSA and RSP. As it will be shown in Section IV-A, we discovered that VIIRS and MODIS have quite comparable BRF precisions for all biomes, which justified that the configuration of MODIS RSP can be inherited by VIIRS. Therefore, the key problem of prototyping the VIIRS LAI/FPAR algorithm is to obtain the SSAs corresponding to VIIRS spectral characteristics. However, direct measurement of SSA at the pixel scale is impossible to implement [33]. Recall that, the objective of the VIIRS mission is to continue the MODIS data record with best consistency. With this aim, we proposed an optimization strategy to locate the optimal VIIRS SSA combination, with the Aqua-MODIS C6 product (MYD15A2H) [57] serving as the benchmark.

There are three reasons justifying the use of MODIS LAI/FPAR retrievals as reference data: 1) ground LAI/FPAR measurements are spatiotemporally limited to solve the optimization problem; 2) MODIS operational algorithm has been well optimized for its BRF inputs; and 3) the ultimate goal is to assure the consistency between VIIRS and MODIS. The performance metrics of the VIIRS LAI/FPAR operational algorithm include: 1) the RI; 2) the root mean squared error (RMSE) between VIIRS and MODIS retrievals; 3) the proximity of the VIIRS and MODIS LAI histograms; and 4) the algorithm match index (AMI). These are defined in the following.

The RI is the percentage of pixels for which the main algorithm produces a retrieval, that is

$$RI = \frac{\text{number of pixels retrieved by the main algorithm}}{\text{number of total processed pixels}}. \quad (4)$$

The RI characterizes the spatial coverage of the best quality and high precision retrievals, but it does not characterize

their accuracies. The RMSE is an accuracy indicator representing the discrepancy between VIIRS retrievals and the reference data

$$RMSE = \sqrt{\frac{1}{N} \sum_{i=1}^N [LAI_{VIIRS}(\omega, i) - LAI_{MODIS}(i)]^2}. \quad (5)$$

The proximity of LAI histograms is another indicator of disagreement, which, in this paper, is quantified by A, P, and U (accuracy, precision, and uncertainty) statistics following Tan *et al.*'s work [56] (Appendix B). Furthermore, the AMI that accounts for the rate of retrieved pixels via the same algorithm path is defined as

$$AMI = \frac{\text{number of retrieved pixels via same algorithm path}}{\text{number of total processed pixels}}. \quad (6)$$

Apparently, the AMI can also magnify the disagreement of two products. These complementary decision rules are employed in addition to the RI and RMSE base rule to mediate the bias problem.

The adjustment procedure can be formulated as follows: find a combination of SSAs at the red ω_{red} and NIR ω_{NIR} spectral bands that: 1) maximizes the RI and the AMI and 2) minimizes the RMSE and the disagreement between the histograms. First, we calculated the RI and RMSE as a function of ω_{red} and ω_{NIR} . Second, we separated a subset of first ten best pairs $(\omega_{red}^1, \omega_{NIR}^1), (\omega_{red}^2, \omega_{NIR}^2), \dots, (\omega_{red}^{10}, \omega_{NIR}^{10})$ rather than using a preset threshold, as the RI and RMSE vary significantly with biome types and sampled data sets. Finally, we selected a pair $(\omega_{red}^i, \omega_{NIR}^i)$ from this subset for which the AMI was maximized and the disagreement of the LAI histograms was minimized. This procedure is illustrated in Fig. 2, taking Biome 6 (deciduous broadleaf forest) as an example. The global best quality MODIS C6 afternoon LAI retrievals (MYD15A2H) generated by the main algorithm for the entire overlapping year 2015 were used as the reference data set. The input land cover (LC) map was the same for MODIS and VIIRS (i.e., three-year dynamic MODIS LC). Note that only these pixels that were retrieved by both the MODIS and VIIRS main algorithm were used to calculate the RMSE and to inspect the proximity of histograms.

C. Generation and Evaluation of VIIRS LAI/FPAR

The VIIRS daily SR product, called VNP09GA, is composed of all available BRF observations for a given day with global coverage [53]. By calculating the quality score of each observation based on QA and geometry information, the algorithm produces the intermediate SR data set that only contains the best quality observation. This is beneficial to minimize the impact of upstream products. The only required ancillary data are global LC classification map (8-biome scheme) as a prior knowledge to solve the ‘‘ill-posed’’ inverse problem.

VIIRS LAI/FPAR production should go through three procedures: algorithm development, product analysis, and validation [25]. This paper analyzes the product performance through a series of comparisons with the MODIS C6 LAI/FPAR data set. We compared the two data sets during the entire year

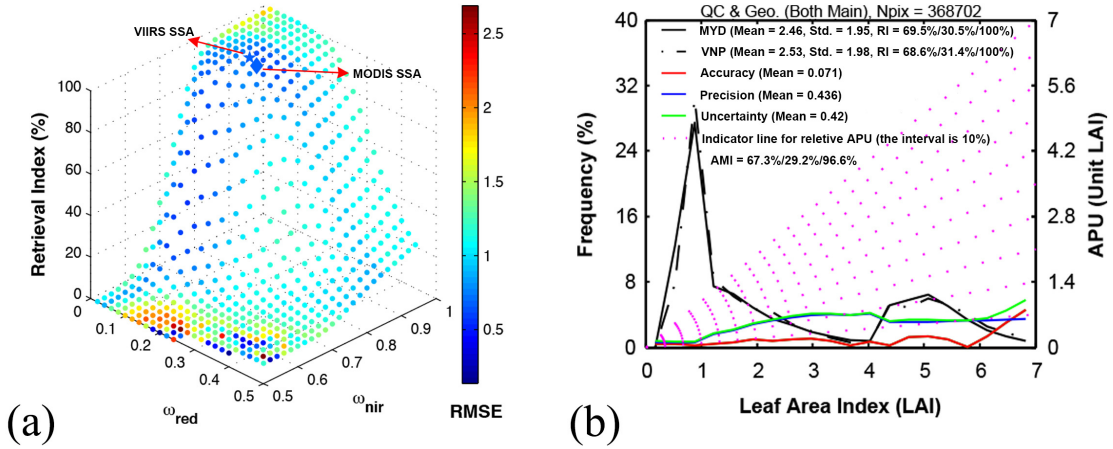


Fig. 2. Illustration of the SSA adjustment approach taking an example for Biome 6. (a) RI [see (4)] and the difference [RMSE (5)] between the MODIS and VIIRS LAI values and as a function of the SSA at the red (ω_{red}) and NIR (ω_{NIR}) spectral bands. Each dot represents a possible combination of the two bands' SSA. The diamond and star markers represent the MODIS-based and optimally selected parametric combinations, respectively. (b) LAI histograms of MODIS and VIIRS with quantified A, P, and U statistics (Appendix B). Because considering only RI and RMSE introduces a biased optimized SSA combination depending on given sample characteristics, we attempted to take account of APU measures. "MYD" and "VNP" stand for Aqua-MODIS LAI and VIIRS LAI, respectively. The mean value, standard deviation, and main algorithm path rates without saturation, with saturation, and both are listed in the plot, respectively. The AMI [see (6)] is additionally used to quantify the agreement. Here, three numbers following "AMI" represent the rates of matched main algorithm path under without saturation (67.3%), saturation (29.2%), and both (96.6%) conditions. In this example, AMI is 96.6% suggesting that only 3.4% of the pair (retrieval and reference) pixels are retrieved through different algorithm paths.

TABLE II
PRECISION COMPARISON BETWEEN MODIS AND VIIRS SR DATA SETS DURING THE PERIOD JULY 4–11, 2015

Biome	B1	B2	B3	B4	B5	B6	B7	B8	Overall
CV _{Red} Difference	0.031	0.007	0.020	0.033	0.003	0.059	0.065	0.030	0.025
CV _{NIR} Difference	0.010	0.001	0.006	0.000	-0.014	0.006	0.034	0.021	0.009

The Coefficient of Variation (CV) is used to quantify the SR precision. Positive values of CV difference mean that VIIRS SR has relative lower precision than MODIS's, vice versa.

of 2015 in terms of spatial distribution, seasonal variation, and main algorithm coverage. The consistency was checked at both global and regional scales. Note that only Aqua-MODIS product was compared with VIIRS's as Aqua and SNPP have a similar satellite transit time.

IV. RESULTS

A. Comparability of Surface Reflectance

1) *Precision Comparability*: In this paper, the SR precision comparability is examined by comparing CVs of the two sensors rather than estimating the RSP, as RSP is not practically measurable. Table II summarizes the results of precision comparison between VIIRS and MODIS BRF data sets. It suggests that overall the VIIRS BRFs have slightly lower precision (the difference of CV is 2.5%) than that of MODIS in the red band, whereas they show a minimal CV difference (less than 1%) in the NIR band. Note that their difference of the red-band (NIR-band) SR precision is a function of biome type and varies between 0.3% (−1.4%) and 6.5% (3.4%). The biome dependence of SR precision can be explained by the usage of an LC map, based on which different parameter configurations are applied in the atmospheric correction process [58]. From this point of view, LAI/FPAR

retrievals should have varying accuracy over different biome types even if the model was ideal. In addition, the red band shows much higher precision differences than NIR band over all biome types except Biome 5 (evergreen broadleaf forest).

Spatial distributions of CV in Fig. 3, taking the tile h17v07 (dominated by grasses/cereal crops) as an example, reveal a strong spatial agreement between MODIS and VIIRS. Both MODIS and VIIRS show relatively more stable (higher precision) SR at the NIR band than at the red band, which supports the previous report in <http://modis-sr.ltdri.org/pages/validation.html>. The observed comparable BRF precisions justify setting the RSP as the same as that used for MODIS LAI/FPAR C6 product.

2) *Surface Reflectance Difference*: All available daily VIIRS and MODIS observations over the globe with the best quality were used to quantify the BRF difference. Table III summarizes the absolute and relative difference of BRFs over the eight biome types. The same as the BRF precision, the magnitude of a BRF difference also varies with biome type. The two sensors have the most comparable BRFs over Biome 2 (shrubs), whereas Biome 5 (evergreen broadleaf forest) shows the largest relative discrepancy. Generally, VIIRS shows relatively lower BRF at the red band (from −13.9%

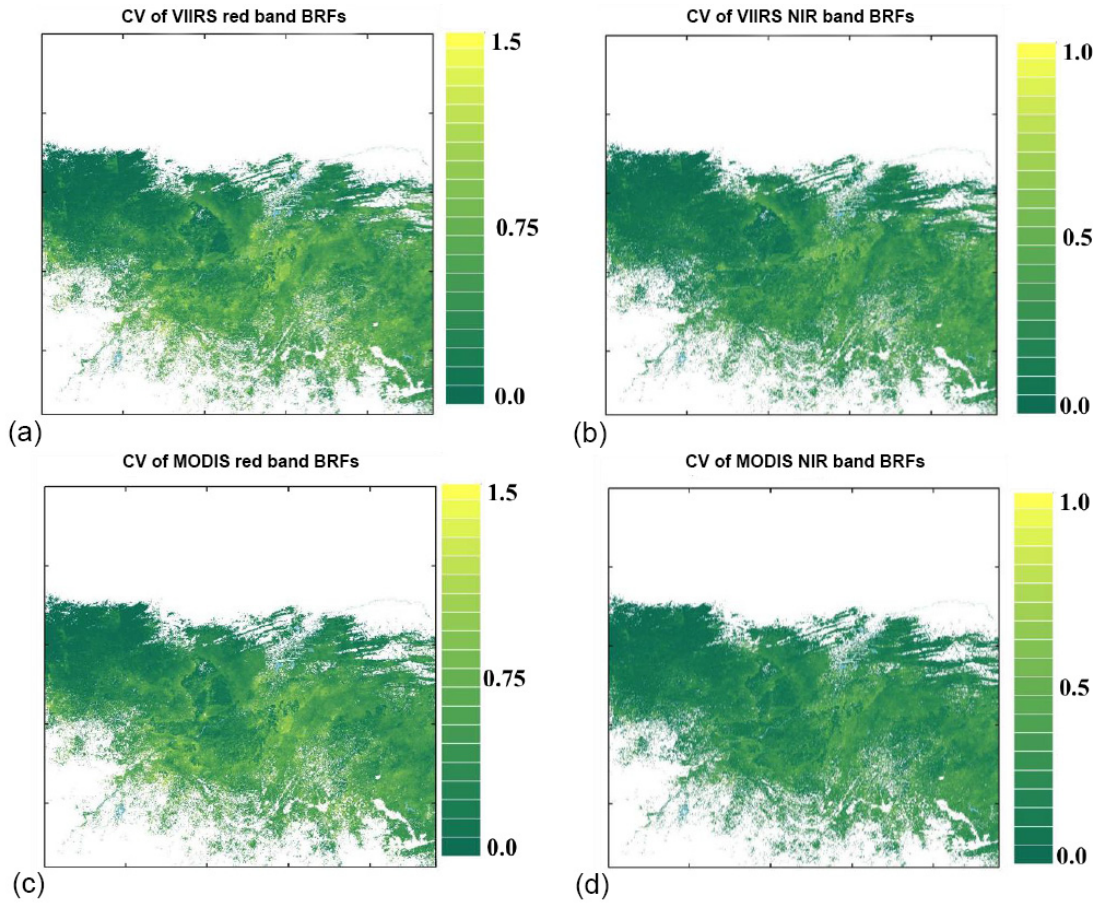


Fig. 3. Spatial distribution of the VIIRS and MODIS BRF precisions quantified by CV. This is an example of Biome 1 (grasses/cereal crops) dominant tile (h17v07). Pixels that were not classified into B1 among these 2400×2400 pixels were masked by white color. CVs of VIIRS BRF at (a) red and (b) NIR bands. CVs of MODIS at (c) red and (d) NIR bands.

TABLE III

COMPARISON BETWEEN VIIRS AND MODIS BRF DATA SETS (VNP09GA AND MYD09GA) OVER THE GLOBE DURING THE PERIOD JULY 4–11, 2015

Biome	B1	B2	B3	B4	B5	B6	B7	B8
$\Delta\text{BRF}_{\text{red}}$	-0.0036	-0.0033	-0.0045	-0.0035	-0.0039	-0.0036	-0.0032	-0.0041
$\Delta\text{BRF}_{\text{NIR}}$	0.0096	0.0088	0.0132	0.0076	0.0158	0.0102	0.0031	0.0027
$\Delta\text{BRF}_{\text{red}}\%$	-3.09	-2.91	-6.13	-5.64	-11.22	-11.21	-9.89	-13.89
$\Delta\text{BRF}_{\text{NIR}}\%$	3.30	3.29	3.84	3.06	4.91	3.43	1.44	1.17

Positive values of BRF median mean that VIIRS has larger reflectance than MODIS, vice versa.

to -2.9%) and higher BRF at the NIR band (1.2% – 4.9%) than MODIS, indicating possible overestimation of LAI/FPAR retrievals and shrinking performance of main algorithm if the MODIS LUT configuration is directly applied to VIIRS. Histograms of absolute BRF differences across all biomes and the relative BRF differences over Biome 6 (deciduous broadleaf forest) are shown in Fig. 4(a) and (b) as an example, respectively. VIIRS shows relatively lower red-band BRFs (-0.0027) and higher NIR-band BRFs (0.0059) than MODIS. These results confirm the findings of the previous study [59]. The obvious BRF shifts in the two bands from MODIS to VIIRS indicate the necessity to do the sensor-specific parametric optimization, as the main objective of this paper.

B. VIIRS-Specific Parameterization

We obtained the biome- and spectral-specific SSAs for VIIRS through the adjustment. Table IV shows the SSA differences between MODIS and VIIRS configurations. VIIRS has smaller SSAs at the red band for all biomes than the heritage MODIS LUTs, but has larger SSAs at the NIR band for most of biomes, except for Biomes 7 and 8 (they have the same SSA). These SSA changes agree well with the shift direction of the BRF reported in Section IV-A, which coincides with the theoretical expectation discussed in Section II-C.

Fig. 5 shows an example (Biome 6) of model-based LUT entries used in the MODIS C6 operational algorithm and adjusted for the VIIRS instrument. For a given LAI and soil pattern, the VIIRS LUT generates slightly lower red-band BRF

TABLE IV
DIFFERENCES OF SSA BETWEEN VIIRS AND MODIS PARAMETRIC CONFIGURATIONS

Biome	B1	B2	B3	B4	B5	B6	B7	B8
ΔSSA_{red}	-0.04	-0.03	-0.05	-0.05	-0.05	-0.02	-0.03	-0.03
ΔSSA_{NIR}	0.01	0.02	0.01	0.01	0.02	0.01	0.00	0.00

Positive values of SSA difference mean that VIIRS has larger SSA than MODIS, vice versa.

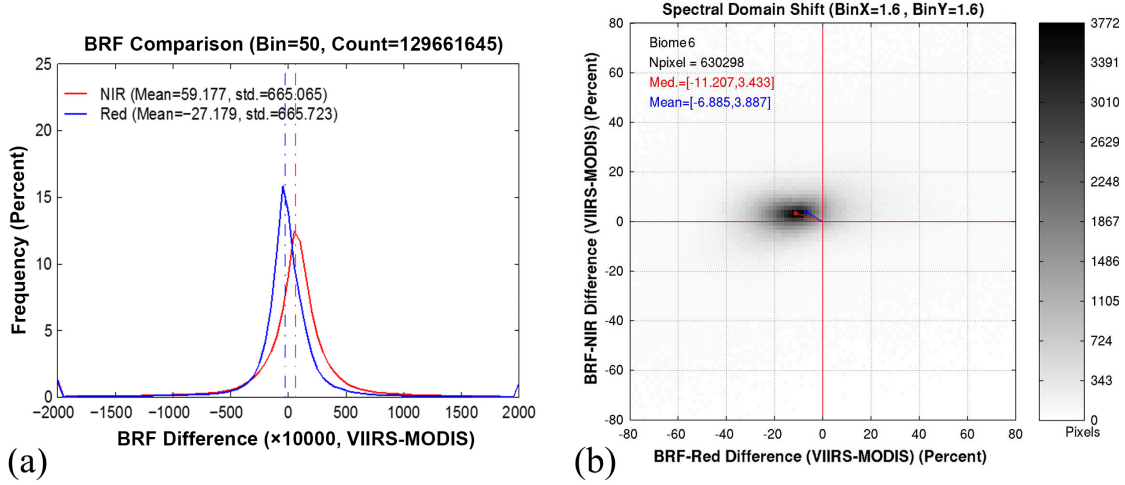


Fig. 4. (a) Histogram of absolute BRF difference at the red and NIR bands across all biomes. A positive difference means that VIIRS BRF is higher than MODIS or vice versa. VIIRS shows relatively lower red-band BRFs (-0.0027) and higher NIR-band BRFs (0.0059) than MODIS. (b) Relative BRF differences over Biome 6 (deciduous broadleaf forest) are plotted in the red–NIR spectral domain. Obvious leftward and upward spectral shifts are observed. The median and mean values of the red- and NIR-band BRF differences are given, respectively. For this comparison, strict quality control and minimal sun-view geometry difference are applied to use only best quality observations.

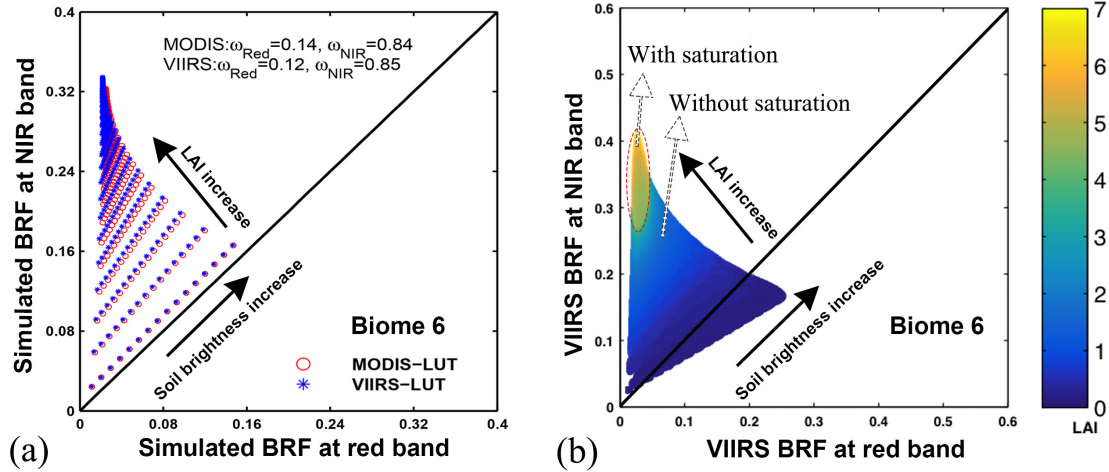


Fig. 5. (a) LUT entries in the red–NIR spectral space configured for MODIS C6 (circle) and VIIRS (asterisk) BRF data sets. Each circle (asterisk) represents a unique solution under a given canopy and soil pattern. For a given LAI and soil pattern, the VIIRS LUT generates slightly lower red-band BRF and higher NIR-band BRF values than MODIS LUT. (b) Retrieval domain of the algorithm calibrated for VIIRS BRF data. The main algorithm retrieves an LAI value only if the observed pair $(BRF_{\text{red}}, BRF_{\text{NIR}})$ of VIIRS BRFs falls within the retrieval domain. The LUT entries and retrieval domain are for deciduous broadleaf forest (Biome 6). The LUT entries and retrieval domain are for broadleaf forests (Biome 6), SZA between 22.5° and 37.5° , view zenith angle between 0° and 8.5° , and the relative azimuth angle between 0° and 25° .

and higher NIR-band BRF values compared with operational MODIS LUT [see Fig. 5(a)]. This agrees with the shift direction of measured BRFs from MODIS and VIIRS [see Fig. 4(a)] and, therefore, means that the proposed adjustment procedures

result in a successful spectral domain shift that enables a VIIRS retrieval comparable with the MODIS product. The retrieval domain is a set of points in the spectral space for which the algorithm retrieves at least one acceptable solution.

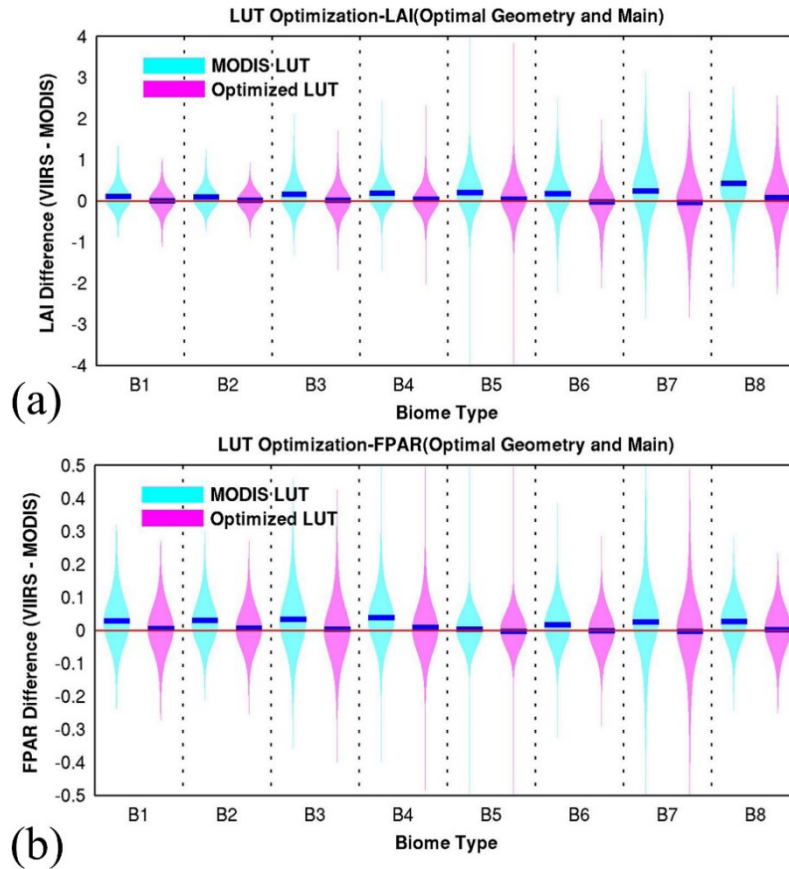


Fig. 6. (a) Distributions of LAI difference (VIIRS-MODIS) before (using MODIS LUT) and after optimization. Global SR and its retrieval during a compositing period (July 4–11) in 2015 are used in this analysis. The cyan and magenta violin plots represent the distributions of LAI difference using the MODIS LUT and the newly optimized VIIRS LUT. The blue line in each violin plot stands for the mean value of differences. (b) Same as (a) but for FPAR.

Recall that, the main algorithm accumulates acceptable solutions, i.e., all canopy/soil parameters for which the observed BRFs agree with the LUT entries within a precision ellipse controlled by RSPs. Thus, the configuration of the retrieval domain is controlled by both the SSA combination and RSPs. In the case of dense canopies, the reflectances saturate, and are therefore weakly sensitive to changes in canopy properties. Fig. 5(b) shows the distribution of VIIRS LAI values in the red–NIR spectral space. The saturated reflectances are shown as a green-to-yellow subset in this retrieval domain.

Fig. 6 shows the distributions of LAI and FPAR differences before (using MODIS LUT) and after optimization over the globally sampled data generated by the main algorithm during a compositing period (July 4–11) in 2015. Note that the results shown here are based on the data used for optimization—thus, further consistency evaluation is required. Direct transplantation of the algorithm without any parameter adjustment results in obvious VIIRS overestimation of both LAI and FPAR. This has been predicted by the theoretical analyses, as detailed in Section II-C. In particular, forest biomes (Biomes 5–8) exhibit larger LAI overestimation (0.174–0.427), whereas nonforest biomes (Biomes 1–4) show relatively higher FPAR disparity (0.030–0.038). The plots also show that the LAI of forest biomes has larger uncertainties than that of nonforest biomes. All results demonstrate that the

implemented optimization and selected parameters successfully reduce differences between MODIS and VIIRS (from 0.146 down to 0.014 for LAI and from 0.030 down to 0.005 for FPAR).

The adjustment procedure also results in the improvement of the main algorithm execution rate, i.e., increasing the RI. Fig. 7 shows the comparison of the algorithm retrieval rates before and after the LUT optimization. Without parametric adjustment, VIIRS shows comparable RIs over nonforest biomes (less by 0.5%–1.7%) but significantly lower RIs in forest biomes (less by 6%–12%). Recall that the RI is a key indicator of the quality of retrievals. Thus, the discrepancy of the two sensors could reduce the quality of retrievals if the LAI/FPAR algorithm was not adjusted. Fig. 7(b) shows that the optimized VIIRS LUT successfully increases the RIs and yields equivalent RIs (within $\pm 1.3\%$) with that of MODIS over all biomes.

V. GLOBAL VIIRS LAI/FPAR

A. Description of VIIRS LAI/FPAR

The VIIRS LAI/FPAR fields are produced daily (VNP15A1) at 500-m spatial resolution and composited to generate the publicly available eight-day product (VNP15A2). The product is projected on the sinusoidal 10° grid, where the globe is

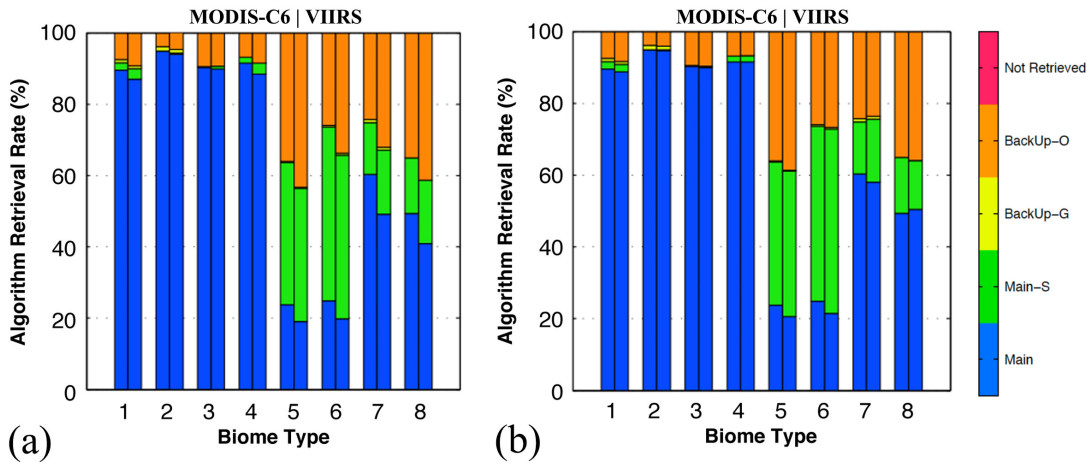


Fig. 7. Algorithm retrieval rate (%) of MODIS C6 (left bars) and VIIRS (right bars) by biome types. (a) Before adjustment. (b) After adjustment. Retrievals during a compositing period (July 4–11) in 2015 are used. Algorithm retrieval rate is defined as the ratio of the number of pixels with LAI and FPAR retrieved by each algorithm path to the total number of retrievals by both the main and backup algorithms.

tiled into 36×18 tiles, each containing 2400×2400 pixels. Note that the HDF-EOS5 data format, replacing MODIS’s HDF-EOS, is used to store six scientific data sets and other information that describes some properties of the data. In general, the VIIRS LAI/FPAR product follows the MODIS C6 LAI/FPAR product [25], and its details can be found in the VIIRS LAI/FPAR Algorithm Theoretical Basis Document [60]. The VIIRS LAI/FPAR product has been generated, since VIIRS started acquiring data in 2011 and will be freely available.

The global distributions of LAI, FPAR, and corresponding algorithm path during two compositing periods in January and July of year 2015 are shown in Fig. 8. As expected from the RT theory, FPAR shows a distribution pattern similar to that of LAI, coinciding closely with the distribution of biome types—high values over forests and low values over herbaceous vegetation. Due to the polar night in Arctic regions, we notice an obvious horizontal line (pixels above this line were not retrieved) at high north latitude in January. The larger use of a backup algorithm may be caused by the data contamination of residual snow. From visual comparison, VIIRS LAI/FPAR shows good agreement with MODIS data set, as presented in [25]. Boreal summer shows higher main algorithm coverage than during boreal winter. The large parts of backup algorithm execution over high north latitudes during boreal winter season are caused by large SZA [see Fig. 8(e)]. The large parts of Backup-O for evergreen broadleaf forest are related to cloud/aerosol contamination [see Fig. 8(e) and (f)]. Note that, although LAI/FPAR values over the globe were generated through different algorithms (main or backup), the spatial consistency of the product is sound enough for most applications related to spatial analysis. This is because the LAI/FPAR-NDVI relationships used for the backup algorithm were extracted from a data set generated from the main RT-based algorithm.

B. Consistency With MODIS LAI/FPAR

1) *Spatial Comparison:* The histograms of LAI differences demonstrate good consistency between MODIS and VIIRS

products in both seasons [see Fig. 9(a) and (b)]. The global mean differences, across all biomes, are 0.024 and 0.029 in January and July, respectively. The largest discrepancy is found in the four forest biomes (Biome 5–8), which means larger uncertainties of LAI. For both LAI and FPAR, the profiles derived from the MODIS and VIIRS products match well at most latitude bands [see Fig. 9(c) and (d)]. In the higher latitudes, the Northern Hemisphere shows clearer seasonality than the Southern Hemisphere, because the dominant biome types in the Southern Hemisphere are savannas, shrubs, and grasses that have smaller seasonal variations than the forests that dominate the Northern Hemisphere. VIIRS overestimates MODIS over tropical latitudes, especially over 5°N – 10°S . This is a result of the difference of algorithm path used in MODIS and VIIRS, as will be further discussed later.

In general, MODIS and VIIRS show similar retrieval rate patterns for all biomes and both periods (see Fig. 10) due to comparable precision in MODIS and VIIRS SR data sets and the same procedure applied to adjust the algorithm. Boreal summer has a higher success rate of the main algorithm than boreal winter, especially for needleleaf forests (Biomes 7 and 8), which show a more than 50% improvement. This difference occurred, because needleleaf forests are located in high-latitude regions, where the SZAs are low in the winter season, which results in a large proportion of the backup algorithm. All biomes have RI that is larger than 60% in the boreal summer season, but biomes, such as needleleaf forest, may have very low RI (less than 20%) in the winter season. Nonforest biomes (Biomes 1–4) show generally higher RI than forest biomes (Biomes 5–8) in both seasons. The RIs of nonforest biomes exceed 50% and 90% in winter and summer seasons, respectively. Forest biomes show a large proportion of retrievals under saturation (Main-S) in the summer season because of SR saturation in dense canopies. This means that the reflectances do not contain sufficient information to localize an LAI value. The proportions of the backup algorithm caused by “other reasons” (BackUp-O) for forest biomes are also obviously high in the summer season, which is related to cloud/aerosol contamination. The reason why some pixels are

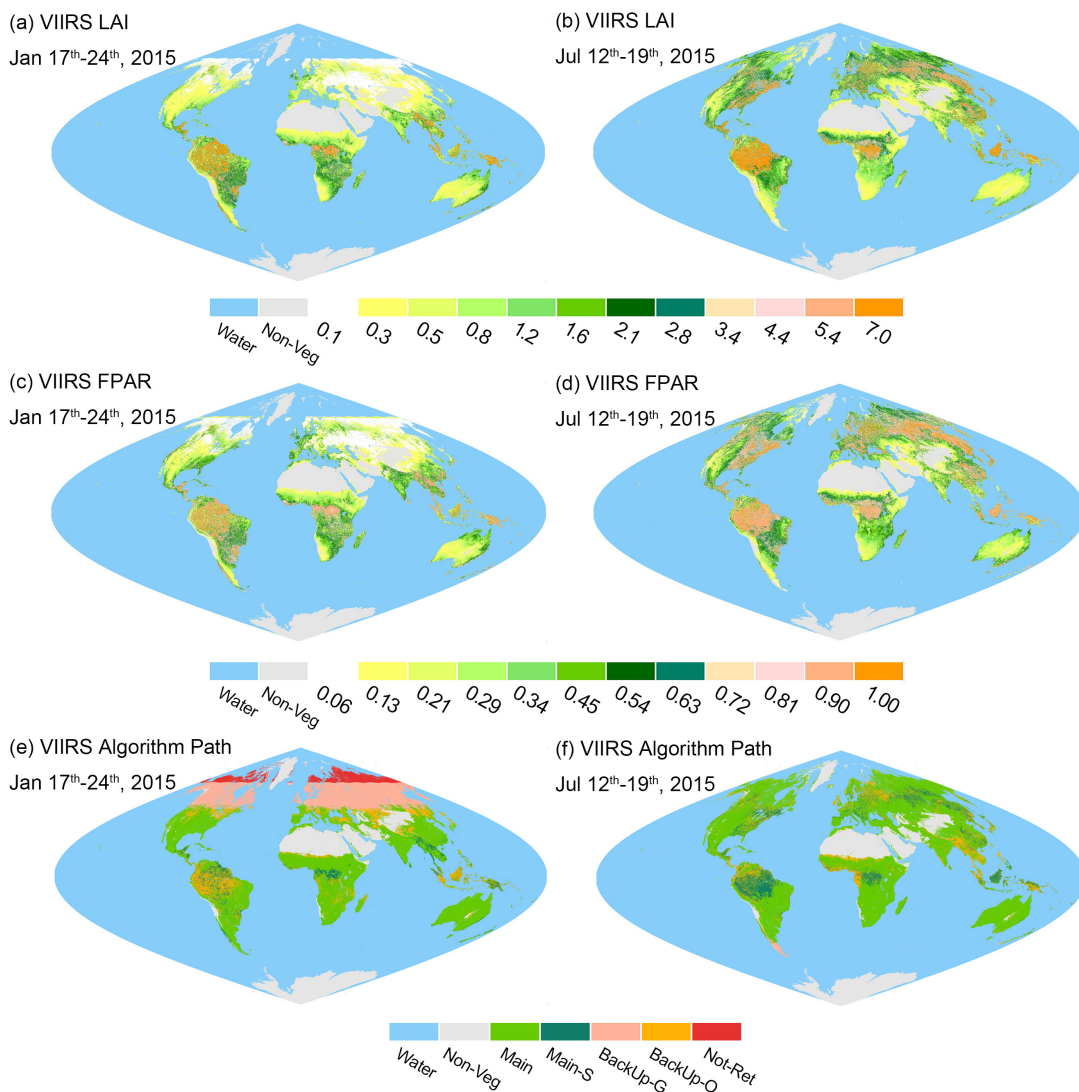


Fig. 8. Global color-coded maps of (a) and (b) SNPP-VIIRS LAI, (c) and (d) FPAR, and (e) and (f) algorithm path during the boreal winter (January 17–24) and summer (July 12–19) of year 2015. In (e) and (f), the term “Main” means the main algorithm without BRF saturation; “Main-S” means the main algorithm with BRF saturation; “BackUp-G” means the backup algorithm caused by large view/SZA; “BackUp-O” means the backup algorithm caused by other reasons; “Not-Ret” means algorithms are not executed, because BRFs are not available. An equal-area sinusoidal projection is used here.

not retrieved in winter season is because of the ice and snow coverage that exists and the low SZA. Thus, the quality of the LAI/FPAR products varies from season to season and biome to biome.

For more detailed compression, the spatial distributions of LAI over the American continent are shown in Fig. 11(a). There is no visually distinguishable difference between the two data sets over the entire continent with absolute differences within ± 0.5 LAI units for most of the land surfaces. However, there are some obvious differences over densely vegetated regions. These discrepancies can exceed 2 LAI units in Amazon rainforests and over the eastern United States. An examination of the details revealed no systematic overestimation or underestimation—the differences are stochastic. To investigate the reasons for these discrepancies, we compared the corresponding spatial distributions of algorithm paths [see Fig. 11(b)]. VIIRS and MODIS have very similar patterns

of algorithm paths over the continent. Main algorithms with and without saturation were used to retrieve LAI for densely vegetated regions and most other regions, respectively. The backup algorithm covers the southern part of South America in both MODIS and VIIRS data, which can be explained by the poor sun-sensor geometry. We see that VIIRS has a slightly higher backup algorithm rate because of “other reasons” than MODIS over the Amazon forests. The fact that the backup algorithm has lower accuracy than the main algorithm explains LAI discrepancies over these regions. This suggests that the input data play an important role in affecting the variation and magnitude of LAI/FPAR retrievals.

2) *Temporal Comparison:* In this section, we compare the seasonality of LAI/FPAR values and algorithm paths from MODIS and VIIRS data sets over two representative tiles. The tiles h11v04 and h12v04, located on both the west and east sides of the Great Lakes region of the United States,

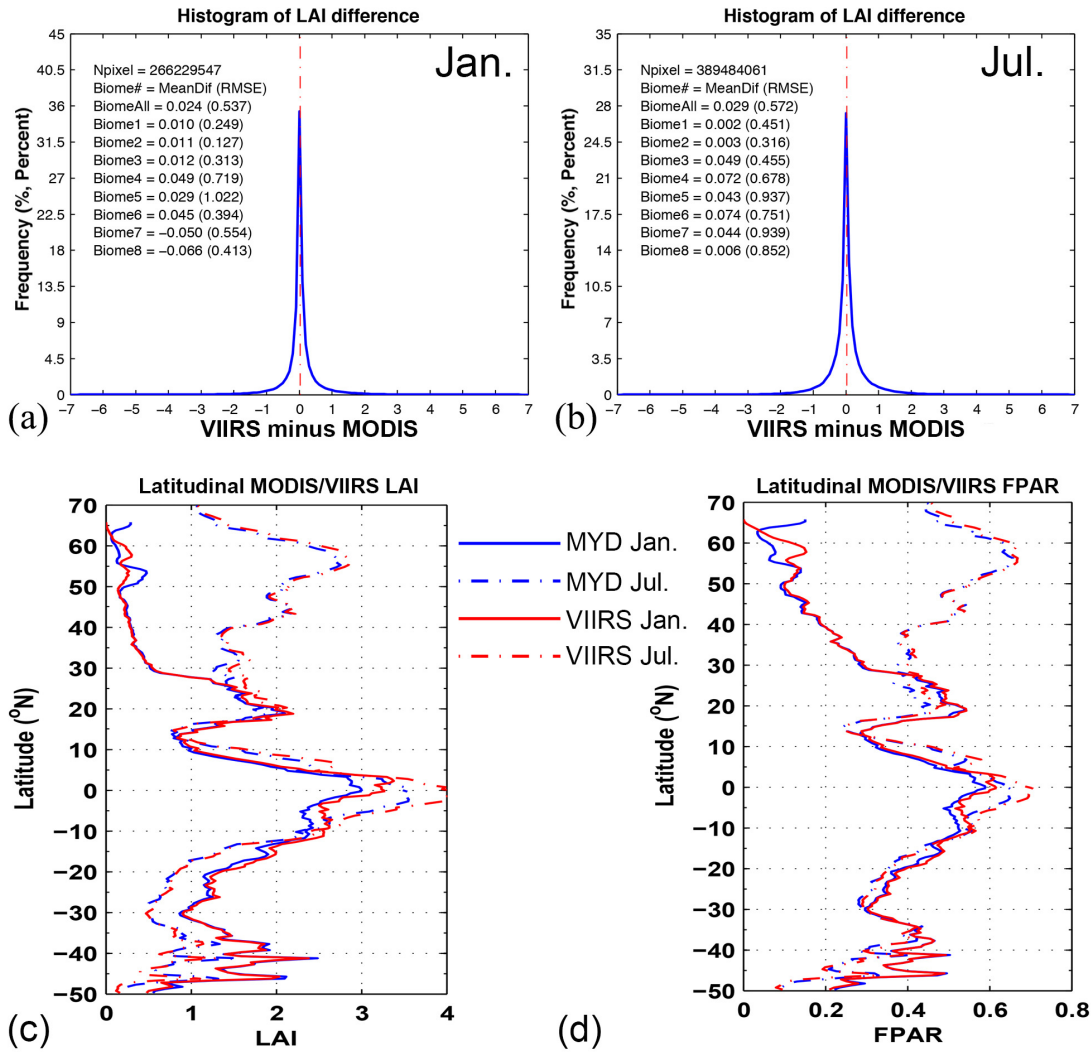


Fig. 9. Comparison between VIIRS and MODIS LAI/FPAR products. (a) Histogram of LAI comparison between MODIS and VIIRS in January. Biome-specific comparison results are also given. (b) Same as (a) but for July. (c) and (d) Latitudinal distributions of global LAI and FPAR, respectively. The latitude interval is 0.1°. Solid and dashed lines depict January and July, respectively.

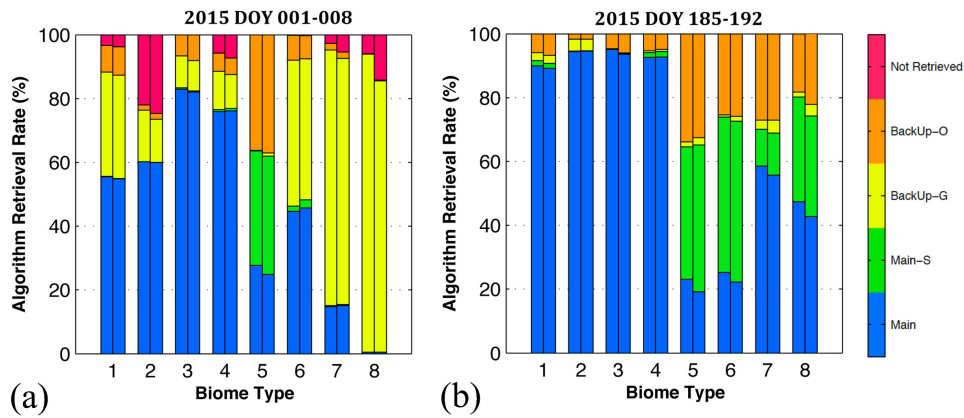


Fig. 10. Retrieval rates of different algorithm paths as a function of biome type at the global scale in (a) boreal winter season and (b) boreal summer season. MODIS (left bars) and VIIRS (right bars) are compared.

are dominated by broadleaf crops (Biome 3) and deciduous broadleaf forest (Biome 6), respectively. The scatter plots in Fig. 12 show a comparison between the MODIS and VIIRS

LAI/FPAR values over the entire year of 2015. The 46 color-coded circles in each plot represent the averaged LAI/FPAR values of all biome-specific pixels during the corresponding

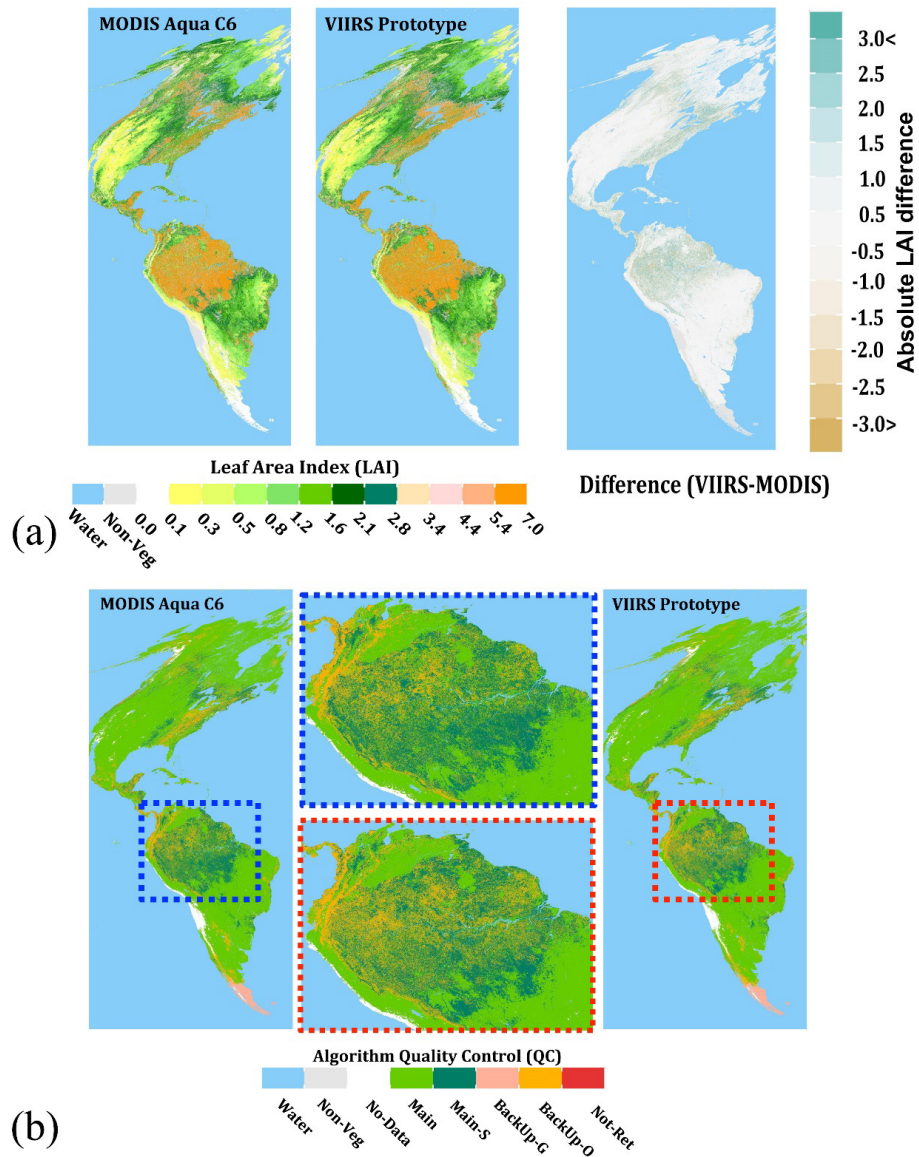


Fig. 11. (a) Comparison of spatial distributions of LAI from MODIS and VIIRS products over the American continent. (b) Comparison of the spatial distributions of algorithm paths corresponding to (a). The two plots in the middle figure show the zoomed-in details over the Amazon rainforests. The data sets are from January 4–11, 2015. An equal-area sinusoidal projection is used here.

eight-day composites. Temporal variations in LAI and FPAR show good consistency. Both LAI and FPAR show clear seasonality of the two biomes. LAI and FPAR increase in spring from low levels in winter and then reach to their peak values in summer. Thereafter, the values decrease in autumn until the next winter.

The LAI/FPAR differences between two neighboring eight-day composites are varying rather than constant, which means that the rate of LAI changes is different from time to time. The larger distances in spring and autumn indicate that the LAI/FPAR changes rapidly in these two seasons, whereas the dense dots especially in the winter season indicate that the LAI/FPAR does not change very much. This phenology is related to the seasonality of the climatic conditions [61], which, as we can see, has been captured by both LAI/FPAR

products. VIIRS LAI and FPAR agree well with MODIS, with R^2 larger than 0.99 for both biomes. There does not seem to be any obvious systematic bias between the two products. The reasonable LAI/FPAR seasonality and good agreement between MODIS and VIIRS imbue confidence in the VIIRS products.

The algorithm paths are of critical importance for retrieval accuracy and could be affected by vegetation density, sun-sensor geometry, and atmospheric conditions. Thus, algorithm path should exhibit seasonality. Fig. 13 shows the annual variation of algorithm retrieval rates over two selected tiles. MODIS and VIIRS are compared in each of the 46 pairs of bars. Clear seasonality of algorithm retrieval rate occurs in both biome types. The RI in the winter season is much lower than that in other seasons because of poor geometry and

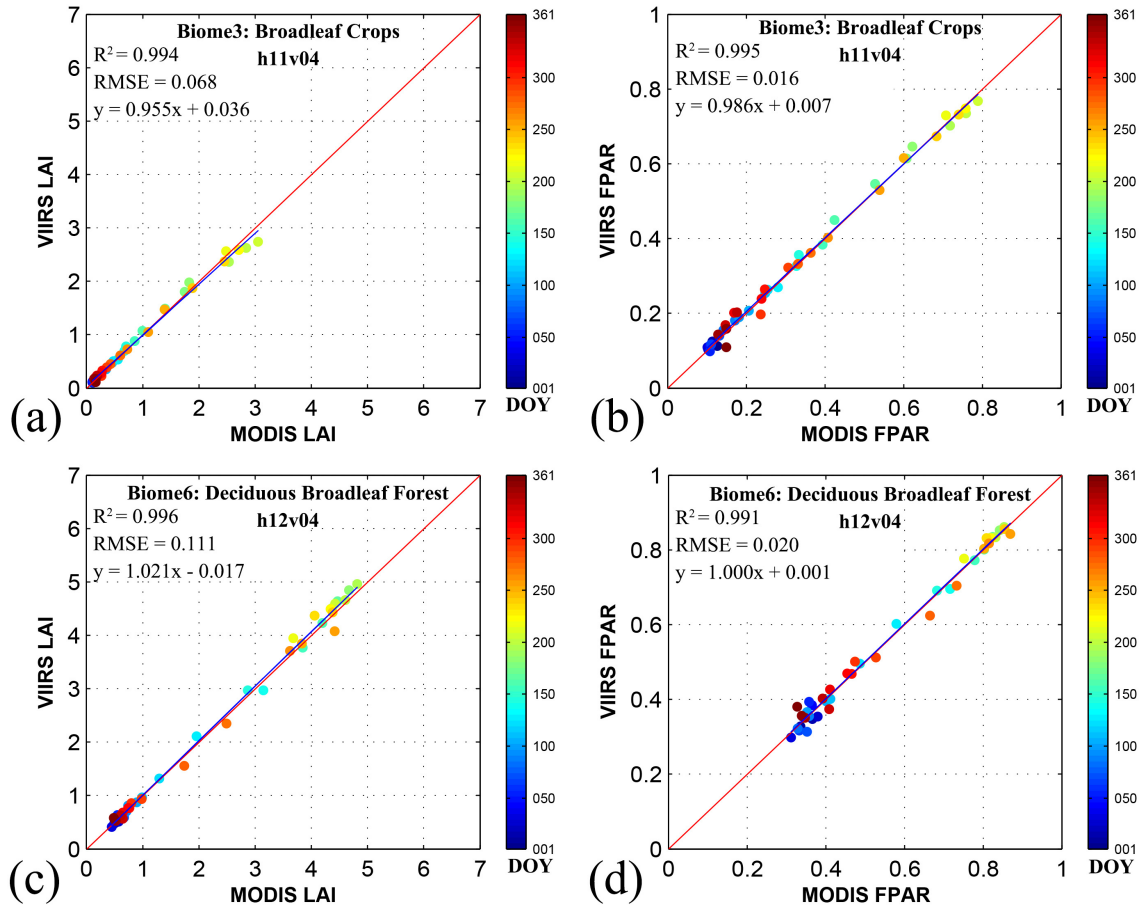


Fig. 12. (a) Comparison between MODIS and VIIRS LAI values over an entire one-year period (2015). Each circle represents the averaged LAI values of all broadleaf crops (Biome 3) pixels in the h11v04 tile and its color stands for the Day of Year. (b) Same as (a) but for FPAR. (c) Same as (a) but for the deciduous broadleaf forest (Biome 6). (d) Same as (b) but for Biome 6.

ice/snow coverage. With less human intervention, the forests show smoother and clearer annual variation than the crops. The crops have a very high main algorithm retrieval rate ($>90\%$) during the growing season. This ensures the high accuracy of the LAI/FPAR retrievals and is meaningful for the use of these products for purposes, such as crop yield estimation [62].

Higher geometry-caused backup algorithm rates are found over crops than over forests in the winter season. This occurred because, in this case study, the forests are located at higher latitudes than the crops and so have larger SZA. The ice/snow coverage in winter and the cloud/aerosol contamination in summer explain failure of the main algorithm in these periods. Comparing VIIRS with MODIS, we find that they are generally consistent during the entire year over both biomes. VIIRS has slightly higher RI in winter but lower RI in summer than MODIS. This may be related to the algorithm adjustment and slight difference of BRDF precision.

C. Other Potential Discrepancies

VIIRS has broader swath coverage than MODIS, which means that more observations during a period of time can be expected from VIIRS. This is beneficial to BRDF/albedo retrieval as the algorithm uses all good quality observations to fit the model [63]. Recall that, the LAI/FPAR algorithm uses

the optimal BRDF observation to calculate the daily intermediate product and employs the maximum FPAR strategy to select the best retrieval from eight days. More valid observations during the repeat cycle mean more candidates for the selection and provide a greater chance for cloudless observation. Thus, the main algorithm retrieval rate should be improved. From Fig. 14(a), we see that the observation numbers from both MODIS and VIIRS increase with the latitude, as expected. However, VIIRS shows a significantly larger observation number than MODIS, and the number of additional observations can be as large as 13 over high latitudes. MODIS has fewer than 16 observations during 16 days (sensor repeat cycle) over 30°N – 30°S , which means that MODIS cannot have the daily full coverage of the globe [64]. On the contrary, VIIRS has more than 18 observations even over the very low latitude bands.

The benefit of the additional observations is noticeable in Fig. 14(b), where the RIs of MODIS and VIIRS are compared. The RI varies with latitude because of the changes of biome type, climatic condition, sun-sensor geometry, and observation number. Although MODIS and VIIRS show similar curves, we notice that VIIRS has better RI than MODIS over most latitudes, especially over 30°N – 30°S . This means that the additional observations are more meaningful over low latitudes, where MODIS has gaps in its daily data set.

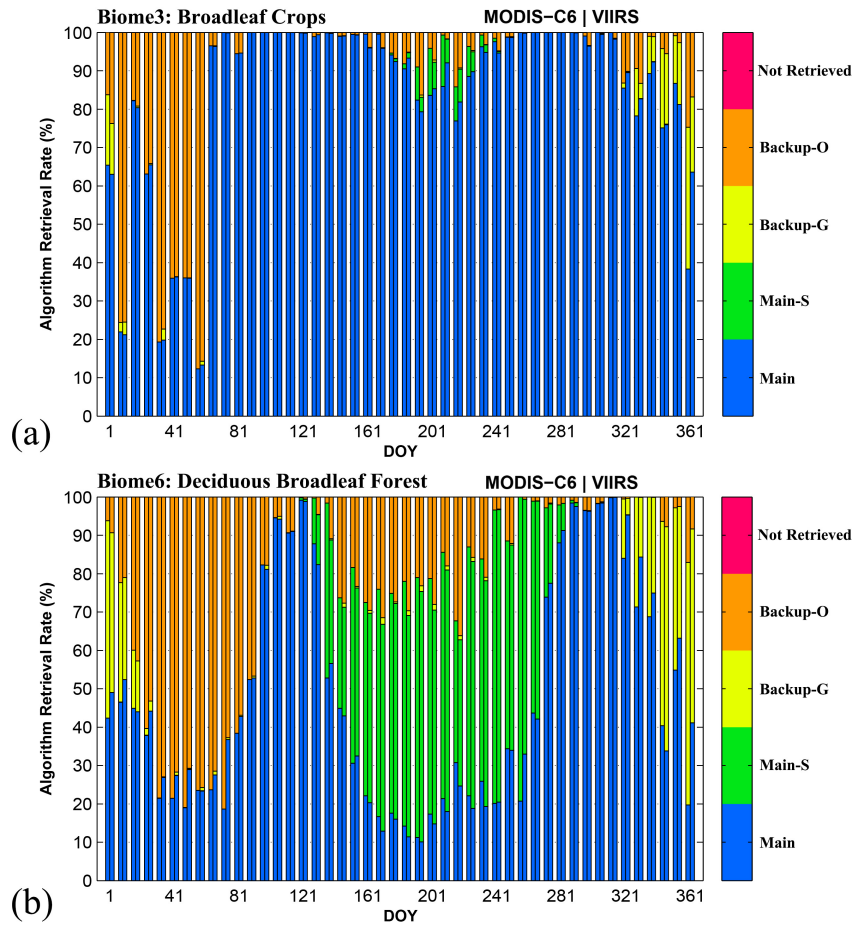


Fig. 13. Annual variation of algorithm retrieval rates (%) in 2015. (a) Algorithm retrieval rates of MODIS (left bars) and VIIRS (right bars) for Biome 3 (broadleaf crops). Consecutive 46 pairs of bar graph demonstrate the seasonal variation of algorithm retrieval rates over the entire one-year period. (b) Same as (a) but for Biome 6 (deciduous broadleaf forest).

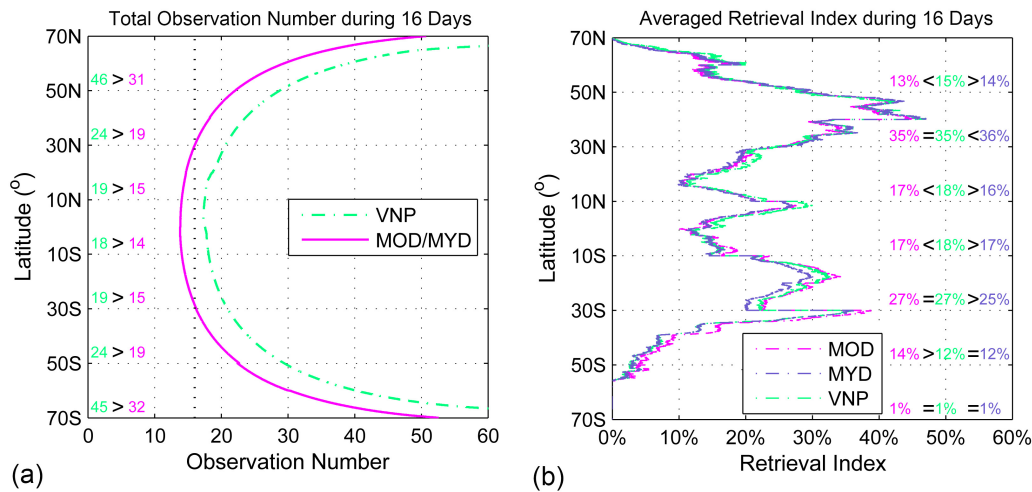


Fig. 14. Comparison of the latitudinal (a) total reflectance observation number during two compositing periods (16 days) and (b) LAI/FPAR RI between VIIRS and MODIS. The total observation numbers during the 16 days near the spring equinox (March 14–29) were extracted from MODIS and VIIRS daily reflectance data. The vertical bold and dotted line in (a) represents 16 observations. The RIs shown in (b) are the mean values of two eight-day composites. “MOD,” “MYD,” and “VNP” represent Terra-MODIS, Aqua-MODIS, and NPP-VIIRS, respectively. The mean values within each 20° of latitude were calculated and compared in the plots.

Over high latitudes, this is not important, because MODIS also has sufficient observations. Although broader coverage makes sense for increasing the RI, a large view angle associated

with such coverage can bring more uncertainties to the retrieval process. We also note that the RIs from Terra- and Aqua-MODIS are not totally consistent. For the Southern

Hemisphere, Terra-MODIS shows obviously larger RI than Aqua-MODIS, which is mostly due to afternoon clouds.

Compared with MODIS, VIIRS has fewer spectral bands [37]. Although the LAI/FPAR algorithm only makes use of two spectral bands, the absence of some other bands can affect the LAI/FPAR product by affecting the quality of upstream products, e.g., SR data set. Compared with MODIS, we notice that some quality assurance flags (e.g., if the pixel is adjacent to cloud) are missing in the VIIRS daily reflectance data. This weaker quality assurance can be transferred to the downstream LAI/FPAR products. From the LAI/FPAR products, we find that VIIRS has slightly larger backup algorithm rate because of quality problems with BRF data. This may be due to two reasons: 1) observations may be contaminated by cloud or aerosol while not detected by the upstream procedure because of fewer spectral bands and 2) VIIRS provides some observations with higher uncertainties related to the larger swath coverage (larger view zenith angle).

VI. CONCLUSION

LAI and FPAR have been derived from MODIS observations since 2000. To ensure continuity of ESDRs, the VIIRS instrument, representing a continuation of MODIS, was launched on board the SNPP satellite. This paper presents an overview of studies related to the VIIRS LAI/FPAR algorithm and its production. We adjusted the configurable parameters of the algorithm to address discrepancies between the two sensors based on the theory of spectral invariants. Compared with MODIS, VIIRS has a set of lower red-band SSA (differences range from 0.02 to 0.05 for eight biomes) and larger NIR-band SSA (differences range from 0 to 0.02 for eight biomes), which coincides with the theoretical prediction. The results presented here show good agreement and consistency between MODIS and VIIRS products (global LAI's RMSE is 0.537 and 0.572 for January and July, respectively). They agree well in terms of both LAI/FPAR spatial and temporal patterns and main algorithm coverage. All of these results imbue confidence in the VIIRS product. However, future validation efforts with the participation by the community-at-large are still necessary to ensure the product quality following the protocols established by the Committee on Earth Observation Satellites. More detailed global and multiyear evaluation and ground-measurements-based validation will be discussed in our following paper.

Note that VIIRS and MODIS achieve the important operational multisensor consistent LAI/FPAR data sets. The algorithm and evaluation strategy used for SNPP-VIIRS can be employed in the subsequent JPSS-VIIRS era, i.e., the algorithm proposed here can be used directly on later VIIRS instruments. If good BRF consistency is not guaranteed, the efforts of this paper can be repeated to find the proper LUT parameters.

APPENDIX

A. Observation and Model Precisions

In this section, we formulate the inverse problem of LAI/FPAR retrieval from atmospherically corrected reflectance. Let r_1, r_2, \dots, r_n be surface BRFs at n spectral

bands obtained by correcting at-sensor radiance for atmospheric effects. The correction technique introduces errors in the SR product. The LAI/FPAR algorithm treats BRFs as independent random variables with finite variances $\sigma_k^2, k = 1, 2, \dots, n$, and assumes that the deviations $\varepsilon_k = (r_k - m_k)/\sigma_k$ follow Gaussian distribution [48]. Here, m_k is the mathematical expectation of r_k , which approximates a true value. The random variable, $\chi_\sigma^2[r - m] = \sum_{k=1}^n ((r_k - m_k)/\sigma_k)^2$, characterizing the proximity of corrected data $r = (r_1, r_2, \dots, r_n)$ to the expected values $m = (m_1, m_2, \dots, m_n)$, has a chi-square distribution. The inequality $\chi_\sigma^2 \leq n$ indicates good precision. We assume that the atmospheric correction algorithm provides BRFs r satisfying $\chi_\sigma^2 \leq n$ with a probability $1 - \alpha$. Dispersions $\sigma = (\sigma_1, \sigma_2, \dots, \sigma_n)$ are observation precisions, i.e., precisions of BRFs. The deviation of m from a true vector is the measurement accuracy, or bias. The uncertainty is defined as the RMSE between the estimated and true values and depends on both accuracy and precision [56].

The LAI/FPAR algorithm compares the measured BRFs, r , with those evaluated from the RT model [65], $r_M = (r_{M,1}, r_{M,2}, \dots, r_{M,n})$. r_M also has errors, which are characterized by $\varepsilon_{M,k} = (r_{M,k} - m_{M,k})/\sigma_{M,k}$. Dispersions $\sigma_M = (\sigma_{M,1}, \sigma_{M,2}, \dots, \sigma_{M,n})$ are model precisions and are determined by the range of natural variation in LAI/FPAR that are not accounted for by the model. Deviations of the model predictions $m_{M,k}$ from true values characterize the model accuracy.

B. Accuracy, Precision, and Uncertainty (A, P, and U)

The proximity of LAI histograms mentioned in Section III-B, in this paper, is quantified by A, P, and U (accuracy, precision, and uncertainty) statistics. The accuracy A, also called bias, is defined as

$$A = |\mu - T| \quad (B1)$$

where μ is the average of all the measured values X_i corresponding to a single true value T . The precision P is defined as the standard deviation of the measurements

$$P = \sqrt{\left[\frac{1}{N-1} \sum_{i=1}^N [X_i - \mu]^2 \right]}. \quad (B2)$$

Considering a number of true values T_k and their estimates Y_k , the uncertainty U , alternatively known as the RMSE [66], is defined as

$$U = \sqrt{\left[\frac{1}{M} \sum_{k=1}^M [Y_k - T_k]^2 \right]}. \quad (B3)$$

ACKNOWLEDGMENT

The authors would like to thank the VIIRS and MODIS science team members for their help. They would also like to thank the anonymous reviewers for their fruitful suggestions.

REFERENCES

- [1] W. L. Barnes, T. S. Pagano, and V. V. Salomonson, "Prelaunch characteristics of the Moderate Resolution Imaging Spectroradiometer (MODIS) on EOS-AM1," *IEEE Trans. Geosci. Remote Sens.*, vol. 36, no. 4, pp. 1088–1100, Jul. 1998.
- [2] C. O. Justice *et al.*, "The Moderate Resolution Imaging Spectroradiometer (MODIS): Land remote sensing for global change research," *IEEE Trans. Geosci. Remote Sens.*, vol. 36, no. 4, pp. 1228–1249, Jul. 1998.
- [3] D. E. Ahl, S. T. Gower, S. N. Burrows, N. V. Shabanov, R. B. Myneni, and Y. Knyazikhin, "Monitoring spring canopy phenology of a deciduous broadleaf forest using MODIS," *Remote Sens. Environ.*, vol. 104, no. 1, pp. 88–95, 2006.
- [4] R. Narasimhan and D. Stow, "Daily MODIS products for analyzing early season vegetation dynamics across the North Slope of Alaska," *Remote Sens. Environ.*, vol. 114, no. 6, pp. 1251–1262, 2010.
- [5] J. Bi *et al.*, "Amazon forests' response to droughts: A perspective from the MAIAC product," *Remote Sens.*, vol. 8, p. 356, 2016.
- [6] C. Justice, A. Belward, J. Morisette, P. Lewis, J. Privette, and F. Baret, "Developments in the 'validation' of satellite sensor products for the study of the land surface," *Int. J. Remote Sens.*, vol. 21, no. 17, pp. 3383–3390, 2000.
- [7] J. T. Morisette, J. L. Privette, and C. O. Justice, "A framework for the validation of MODIS Land products," *Remote Sens. Environ.*, vol. 83, nos. 1–2, pp. 77–96, 2002.
- [8] X. Xiong, A. Angal, A. Wu, W. Barnes, and V. Salomonson, "Terra and Aqua MODIS instrument performance," in *Proc. IEEE Int. Geosci. Remote Sens. Symp. (IGARSS)*, Jul. 2016, pp. 7388–7391.
- [9] K. Thome and R. Wolfe, "Terra status update including end of mission orbit," in *Proc. MODIS/VIIRS Sci. Team Meeting*, Silver Spring, MD, USA, Jun. 2016. [Online]. Available: https://modis.gsfc.nasa.gov/sci_team/meetings/201606/presentations/plenary/wolfe.pdf
- [10] R. E. Murphy *et al.*, "Using VIIRS to provide data continuity with MODIS," in *Proc. IEEE Int. Geosci. Remote Sens. Symp. (IGARSS)*, Jul. 2001, pp. 1212–1214.
- [11] R. E. Murphy, P. Ardanuy, F. J. Deluccia, J. E. Clement, and C. F. Schueler, "The visible infrared imaging radiometer suite," in *Earth Science Satellite Remote Sensing*. Berlin, Germany: Springer, 2006, pp. 199–223.
- [12] C. Cao, F. J. De Luccia, X. Xiong, R. Wolfe, and F. Weng, "Early on-orbit performance of the visible infrared imaging radiometer suite onboard the Suomi National Polar-Orbiting Partnership (S-NPP) satellite," *IEEE Trans. Geosci. Remote Sens.*, vol. 52, no. 2, pp. 1142–1156, Feb. 2014.
- [13] M. D. Goldberg, H. Kilcoyne, H. Cikanek, and A. Mehta, "Joint Polar Satellite System: The United States next generation civilian polar-orbiting environmental satellite system," *J. Geophys. Res., Atmos.*, vol. 118, no. 24, pp. 13463–13475, 2013.
- [14] B. Yang *et al.*, "Estimation of leaf area index and its sunlit portion from DSCOVR EPIC data: Theoretical basis," *Remote Sens. Environ.*, vol. 198, pp. 69–84, Sep. 2017.
- [15] R. B. Myneni and D. L. Williams, "On the relationship between FAPAR and NDVI," *Remote Sens. Environ.*, vol. 49, no. 3, pp. 200–211, 1994.
- [16] P. J. Sellers *et al.*, "Modeling the exchanges of energy, water, and carbon between continents and the atmosphere," *Science*, vol. 275, no. 5299, pp. 502–509, 1997.
- [17] W. Knorr and J. Kattge, "Inversion of terrestrial ecosystem model parameter values against eddy covariance measurements by Monte Carlo sampling," *Global Change Biol.*, vol. 11, no. 8, pp. 1333–1351, 2005.
- [18] A. D. Richardson *et al.*, "Terrestrial biosphere models need better representation of vegetation phenology: Results from the North American Carbon Program Site Synthesis," *Global Change Biol.*, vol. 18, no. 2, pp. 566–584, 2012.
- [19] S. Garrigues *et al.*, "Validation and intercomparison of global Leaf Area Index products derived from remote sensing data," *J. Geophys. Res.*, vol. 113, p. G02028, Jun. 2008.
- [20] H. Fang *et al.*, "Characterization and intercomparison of global moderate resolution Leaf Area Index (LAI) products: Analysis of climatologies and theoretical uncertainties," *J. Geophys. Res., Biogeosci.*, vol. 118, no. 2, pp. 529–548, 2013.
- [21] Z. Zhu *et al.*, "Global data sets of vegetation Leaf Area Index (LAI)3G and Fraction of Photosynthetically Active Radiation (FPAR)3G derived from Global Inventory Modeling and Mapping Studies (GIMMS) Normalized Difference Vegetation Index (NDVI3G) for the period 1981 to 2011," *Remote Sens.*, vol. 5, no. 2, pp. 927–948, 2013.
- [22] Z. Xiao *et al.*, "Use of general regression neural networks for generating the GLASS Leaf Area Index product from time-series MODIS surface reflectance," *IEEE Trans. Geosci. Remote Sens.*, vol. 52, no. 1, pp. 209–223, Jan. 2014.
- [23] F. Baret *et al.*, "LAI, fAPAR and fCover CYCLOPES global products derived from VEGETATION: Part 1: Principles of the algorithm," *Remote Sens. Environ.*, vol. 110, no. 3, pp. 275–286, 2007.
- [24] F. Baret *et al.*, "GEOV1: LAI and FAPAR essential climate variables and FCOVER global time series capitalizing over existing products. Part1: Principles of development and production," *Remote Sens. Environ.*, vol. 137, pp. 299–309, Oct. 2013.
- [25] K. Yan *et al.*, "Evaluation of MODIS LAI/FPAR product collection 6. Part 1: Consistency and improvements," *Remote Sens.*, vol. 8, no. 5, p. 359, 2016.
- [26] K. Yan *et al.*, "Evaluation of MODIS LAI/FPAR product collection 6. Part 2: Validation and intercomparison," *Remote Sens.*, vol. 8, no. 6, p. 460, 2016.
- [27] S. Hook *et al.* (2012). *An Evaluation of the Suomi-NPP Visible Infrared Imaging Radiometer Suite (VIIRS) and the Associated Environmental Data Records for Land Science After Early Evaluation on on-Orbit Performance*. [Online]. Available: <https://pdfs.semanticscholar.org/76b8/de3775f02465c8e7b2f0932e0283829d1c02.pdf>
- [28] D. Hillger *et al.*, "First-light imagery from Suomi NPP VIIRS," *Bull. Amer. Meteorol. Soc.*, vol. 94, no. 7, pp. 1019–1029, 2013.
- [29] H. Liu *et al.*, "Preliminary evaluation of S-NPP VIIRS aerosol optical thickness," *J. Geophys. Res., Atmos.*, vol. 119, no. 7, pp. 3942–3962, 2014.
- [30] Y. Knyazikhin *et al.*, *MODIS Leaf Area Index (LAI) and Fraction of Photosynthetically Active Radiation Absorbed by Vegetation (FPAR) Product (MOD15) Algorithm Theoretical Basis Document*, document 20771, NASA Goddard Space Flight Center, Greenbelt, MD, USA, 1999.
- [31] Y. Tian *et al.*, "Prototyping of MODIS LAI and FPAR algorithm with LASUR and LANDSAT data," *IEEE Trans. Geosci. Remote Sens.*, vol. 38, no. 5, pp. 2387–2401, Sep. 2000.
- [32] S. Ganguly *et al.*, "Generating vegetation Leaf Area Index earth system data record from multiple sensors. Part 1: Theory," *Remote Sens. Environ.*, vol. 112, no. 12, pp. 4333–4343, 2008.
- [33] S. Ganguly *et al.*, "Generating vegetation Leaf Area Index earth system data record from multiple sensors. Part 2: Implementation, analysis and validation," *Remote Sens. Environ.*, vol. 112, no. 12, pp. 4318–4332, 2008.
- [34] R. B. Myneni *et al.*, "Global products of vegetation leaf area and fraction absorbed PAR from year one of MODIS data," *Remote Sens. Environ.*, vol. 83, pp. 214–231, Nov. 2002.
- [35] W. Yang *et al.*, "Analysis of Leaf Area Index and fraction of PAR absorbed by vegetation products from the terra MODIS sensor: 2000–2005," *IEEE Trans. Geosci. Remote Sens.*, vol. 44, no. 7, pp. 1829–1842, Jul. 2006.
- [36] W. Yang *et al.*, "Analysis of Leaf Area Index products from combination of MODIS Terra and Aqua data," *Remote Sens. Environ.*, vol. 104, pp. 297–312, Oct. 2006.
- [37] X. Xiong *et al.*, "VIIRS on-orbit calibration methodology and performance," *J. Geophys. Res., Atmos.*, vol. 119, no. 9, pp. 5065–5078, 2014.
- [38] R. E. Wolfe, G. Lin, M. Nishihama, K. P. Tewari, J. C. Tilton, and A. R. Isaacman, "Suomi NPP VIIRS prelaunch and on-orbit geometric calibration and characterization," *J. Geophys. Res., Atmos.*, vol. 118, no. 20, pp. 11508–11521, 2013.
- [39] C. F. Schueler, T. F. Lee, and S. D. Miller, "VIIRS constant spatial-resolution advantages," *Int. J. Remote Sens.*, vol. 34, no. 16, pp. 5761–5777, 2013.
- [40] P. Stenberg, M. Möttus, and M. Rautiainen, "Photon recollision probability in modelling the radiation regime of canopies—A review," *Remote Sens. Environ.*, vol. 183, pp. 98–108, Sep. 2016.
- [41] Y. Knyazikhin, A. Marshak, and R. B. Myneni, "3D radiative transfer in vegetation canopies and cloud-vegetation interaction," in *3D Radiative Transfer in Cloudy Atmospheres*. Berlin, Germany, 2005, pp. 617–651.
- [42] Y. Knyazikhin *et al.*, "Estimation of vegetation canopy Leaf Area Index and fraction of absorbed photosynthetically active radiation from atmosphere-corrected MISR data," *J. Geophys. Res.*, vol. 103, pp. 32239–32256, Dec. 1998.
- [43] S. Smolander and P. Stenberg, "Simple parameterizations of the radiation budget of uniform broadleaved and coniferous canopies," *Remote Sens. Environ.*, vol. 94, pp. 355–363, Feb. 2005.
- [44] Y. Knyazikhin *et al.*, "Hyperspectral remote sensing of foliar nitrogen content," *Proc. Nat. Acad. Sci. USA*, vol. 110, no. 3, pp. E185–E192, 2013.

- [45] P. Stenberg, "Simple analytical formula for calculating average photon recollision probability in vegetation canopies," *Remote Sens. Environ.*, vol. 109, no. 2, pp. 221–224, 2007.
- [46] Y. Wang *et al.*, "A new parameterization of canopy spectral response to incident solar radiation: Case study with hyperspectral data from pine dominant forest," *Remote Sens. Environ.*, vol. 85, no. 3, pp. 304–315, 2003.
- [47] M. Möttus and P. Stenberg, "A simple parameterization of canopy reflectance using photon recollision probability," *Remote Sens. Environ.*, vol. 112, no. 4, pp. 1545–1551, 2008.
- [48] Y. Wang *et al.*, "Investigation of product accuracy as a function of input and model uncertainties: Case study with SeaWiFS and MODIS LAI/FPAR algorithm," *Remote Sens. Environ.*, vol. 78, no. 3, pp. 299–313, 2001.
- [49] Y. Knyazikhin, J. V. Martonchik, R. B. Myneni, D. J. Diner, and S. W. Running, "Synergistic algorithm for estimating vegetation canopy Leaf Area Index and fraction of absorbed photosynthetically active radiation from MODIS and MISR data," *J. Geophys. Res., Atmos.*, vol. 103, pp. 32257–32275, Dec. 1998.
- [50] I. N. Bronshtein and K. A. Semendyayev, *Handbook of Mathematics*. Berlin, Germany: Springer, 2013.
- [51] C. Chen *et al.*, "Prototyping of LAI and FPAR retrievals from MODIS multi-angle implementation of atmospheric correction (MAIAC) data," *Remote Sens.*, vol. 9, no. 4, p. 370, 2017.
- [52] A. N. Tikhonov, A. V. Goncharov, V. V. Stepanov, and A. G. Yagola, *Numerical Methods for the Solution of Ill-Posed Problems*, vol. 328. Berlin, Germany: Springer, 2013.
- [53] E. Vermote and B. Franch, "VNP09GA: VIIRS/NPP Surface Reflectance daily L2G global 1 km and 500 m SIN grid V001," NASA EOSDIS Land Process. DAAC, Tech. Rep., 2017. [Online]. Available: https://lpdaac.usgs.gov/dataset_discovery/viirs/viirs_products_table/vnp09ga_v001
- [54] E. Vermote and R. E. Wolfe, "MYD09GA: MODIS/Aqua Surface Reflectance daily L2G global 1 km and 500 m SIN grid V006," NASA EOSDIS Land Process. DAAC, Tech. Rep., 2015. [Online]. Available: https://lpdaac.usgs.gov/dataset_discovery/modis/modis_products_table/myd09ga
- [55] J. Hu *et al.*, "Performance of the MISR LAI and FPAR algorithm: A case study in Africa," *Remote Sens. Environ.*, vol. 88, pp. 324–340, Dec. 2003.
- [56] B. Tan *et al.*, "Validation of Moderate Resolution Imaging Spectroradiometer Leaf Area Index product in croplands of Alpes, France," *J. Geophys. Res., Atmos.*, vol. 110, p. D01107, Jan. 2005.
- [57] R. Myneni, Y. Knyazikhin, and T. Park, "MYD15A2H MODIS/Aqua Leaf Area Index/FPAR 8-day L4 global 500 m SIN grid V006," NASA EOSDIS Land Process. DAAC, Tech. Rep., 2015. [Online]. Available: https://lpdaac.usgs.gov/dataset_discovery/modis/modis_products_table/myd15a2h_v006
- [58] E. F. Vermote and A. Vermeulen, *Atmospheric Correction Algorithm: Spectral Reflectances (MOD09), Version 4.0*, ATBD, 1999. [Online]. Available: http://dratmos.geog.umd.edu/files/pdf/atbd_mod09.pdf
- [59] K. Obata, T. Miura, H. Yoshioka, and A. R. Huete, "Derivation of a MODIS-compatible enhanced vegetation index from visible infrared imaging radiometer suite spectral reflectances using vegetation isoline equations," *J. Appl. Remote Sens.*, vol. 7, no. 1, p. 073467, 2013.
- [60] T. Park, K. Yan, C. Chen, B. Xu, Y. Knyazikhin, and M. Ranga. (2017). *VIIRS Leaf Area Index (LAI) and Fraction of Photosynthetically Active Radiation Absorbed by Vegetation (FPAR) Product Algorithm Theoretical Basis Document (ATBD)*. [Online]. Available: https://viirsland.gsfc.nasa.gov/PDF/VIIRS_LAI_ATBD_V1.0_19Jun2017.pdf
- [61] T. Park *et al.*, "Changes in growing season duration and productivity of northern vegetation inferred from long-term remote sensing data," *Environ. Res. Lett.*, vol. 11, no. 8, p. 84001, 2016.
- [62] P. C. Doraiswamy, J. L. Hatfield, T. J. Jackson, B. Akhmedov, J. Prueger, and A. Stern, "Crop condition and yield simulations using Landsat and MODIS," *Remote Sens. Environ.*, vol. 92, no. 4, pp. 548–559, 2004.
- [63] M. L. Campagnolo, Q. Sun, Y. Liu, C. Schaaf, Z. Wang, and M. O. Román, "Estimating the effective spatial resolution of the operational BRDF, albedo, and nadir reflectance products from MODIS and VIIRS," *Remote Sens. Environ.*, vol. 175, pp. 52–64, Mar. 2016.
- [64] D. Hillger, C. Seaman, C. Liang, S. Miller, D. Lindsey, and T. Kopp, "Suomi NPP VIIRS imagery evaluation," *J. Geophys. Res., Atmos.*, vol. 119, no. 11, pp. 6440–6455, 2014.
- [65] G. Yin *et al.*, "Regional leaf area index retrieval based on remote sensing: The role of radiative transfer model selection," *Remote Sens.*, vol. 7, no. 4, pp. 4604–4625, 2015.
- [66] Y. Zeng *et al.*, "An iterative BRDF/NDVI inversion algorithm based on a posteriori variance estimation of observation errors," *IEEE Trans. Geosci. Remote Sens.*, vol. 54, no. 11, pp. 6481–6496, Nov. 2016



and the generation and assessment of global LAI/FPAR products.

Kai Yan received the B.S. degree in mapping and surveying from the Beijing University of Civil Engineering and Architecture, Beijing, China, in 2011. He is currently pursuing the Ph.D. degree with Beijing Normal University, Beijing.

He was a two-year Visiting Scholar with the Department of Earth and Environment, Boston University, Boston, MA, USA, from 2014 to 2016. His research interests include the BRDF modeling and leaf area index/fraction of photosynthetically active radiation (LAI/FPAR) retrieval over mountain area,



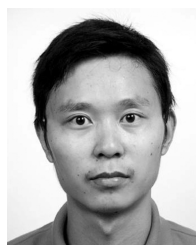
Taejin Park is currently pursuing the Ph.D. degree in geography with the Department of Earth and Environment, Boston University, Boston, MA, USA.

His research interests include the remote sensing of vegetation and climate-vegetation interactions.



Chi Chen received the B.S. degree in remote sensing from Wuhan University, Wuhan, China, in 2013, and the M.A. degree in environmental remote sensing and geographical information system from Boston University, Boston, MA, USA, in 2015, where he is currently pursuing the Ph.D. degree in geography with the Department of Earth and Environment.

His research interests include radiative transfer modeling in land remote sensing, vegetation dynamics, land-atmosphere models and interactions, and climate change.



Baodong Xu received the B.S. degree from Huazhong Agricultural University, Wuhan, China, in 2012. He is currently pursuing the Ph.D. degree with the University of Chinese Academy of Sciences, Beijing, China.

He is currently a Visiting Scholar at Boston University, Boston, MA, USA. His research interests include the validation and uncertainty analysis of remotely sensed leaf area index (LAI) product and LAI inversion over heterogeneous area.



Wanjuan Song is currently pursuing the Ph.D. degree with Beijing Normal University, Beijing, China.

Her research interests include remote sensing modeling, vegetation structure estimation, and DSCOVR EPIC data application.



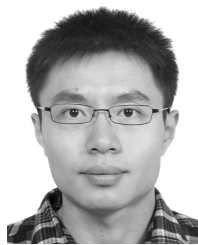
Bin Yang received the Ph.D. degree in photogrammetry and remote sensing from the School of Earth and Space Sciences, Peking University, Beijing, China, in 2017.

He is currently an Assistant Professor with the College of Electrical and Information Engineering, Hunan University, Changsha, China. His research interests include forward and inverse radiative transfer and polarimetric remote sensing.



Guangjian Yan received the Ph.D. degree from the Institute of Remote Sensing Applications, Chinese Academy of Sciences, Beijing, China, in 1999.

He is currently a Professor with the State Key Laboratory of Remote Sensing Science, School of Geography, Beijing Normal University, Beijing. He has authored or co-authored over 160 papers. His research interests include multiangular remote sensing, vegetation remote sensing, radiation budget, scale effect, and scale correction of remote sensing.



Yelu Zeng received the B.S. degree in remote sensing from Wuhan University, Wuhan, China, in 2011, and the Ph.D. degree with the Institute of Remote Sensing and Digital Earth, Chinese Academy of Sciences, Beijing, China, in 2016.

He is currently a Post-Doctoral Research Fellow with the Carnegie Institution for Science, Stanford, CA, USA. His research interests include the 3-D radiative transfer modeling over heterogeneous vegetation canopies, the extraction of vegetation biophysical parameters, such as leaf area index (LAI),

from satellite remote sensing data, the field LAI measurements, and the validation of remotely sensed LAI products.

Yuri Knyazikhin received the M.S. degree in applied mathematics from Tartu University, Tartu, Estonia, in 1978, and the Ph.D. degree in numerical analysis from the N. I. Muskhelishvili Institute of Computing Mathematics, Georgian Academy of Sciences, Tbilisi, Georgia, in 1985.

He was a Research Scientist with the Institute of Astrophysics and Atmospheric Physics, Tartu University, Tartu, Estonia, and the Computer Center of the Siberian Branch, Russian Academy of Sciences, Moscow, Russia, from 1978 to 1990. He was an Alexander von Humboldt Fellow from 1990 to 1996. He is currently a Research Professor with the Department of Geography, Boston University, Boston, MA, USA. His work was published in the areas of numerical integral and differential equations, theory of radiative transfer in atmospheres and plant canopies, remote sensing of the atmosphere and plant canopies, ground-based radiation measurements, forest ecosystem dynamics, and modeling multifunctional forest management.



Zhao Liu received the Ph.D. degree from Beijing Normal University, Beijing, China.

Her research interests include climate change, global warming, and heat wave effect on human health.



Ranga B. Myneni received the Ph.D. degree in biology from the University of Antwerp, Antwerp, Belgium.

He is currently a Professor with Boston University, Boston, MA, USA. He is a Science Team Member of NASA MODIS and VIIRS projects. He has authored or co-authored over 250 scientific articles in peer-refereed journals. His research interests include remote sensing of vegetation and climate-vegetation interactions.